UNIVERSITY OF CALIFORNIA,
IRVINE

# Dealloying Porous Copper and Its Application

THESIS

submitted in partial satisfaction of the requirements
for the degree of

MASTER OF SCIENCE

in Materials Science and Engineering

by

Bowen Shao

Thesis Committee:
Professor Yoonjin Won, Chair
Professor James Earthman
Professor Allon Hochbaum

2018

# DEDICATION

To

my parents and Yihan
for their love and support

# TABLE OF CONTENTS

# LIST OF FIGURES

# LIST OF TABLES

# ACKNOWLEDGMENTS

First of all, I would like to express my deepest appreciation to my advisor, Professor Yoonjin Won, for her guidance and support through my master study and research. Her patience and immense knowledge has been guiding me to the success of my master study and research. Without her advice and guidance, it would be not possible for me to complete this thesis work. Her suggestions and encouragement in the past two years will have huge impact on my life in the future as well.

I would like to thank my committee members, Professor Allon Hochbaum and Professor James Earthman, whose kind help and suggestion inspired me to complete this thesis work.

I also appreciate the people in Won Lab, who supported me and helped me through my thesis work.

I am grateful for the eternal love from my beloved parents, who have been keeping the faith with my academic endeavor at the University of California, Irvine. Their infinite support for me always motivates me to push the limit of myself. This thesis, and all of my accomplishments are rewards to their unconditional love.

# ABSTRACT OF THE THESIS

Dealloying Porous Copper and Its Application

By

Bowen Shao

Master of Science

in Materials Science and Engineering

University of California, Irvine, 2018

Professor Yoonjin Won Irvine, Chair

Frosting process is an inevitable phenomenon in numerous applications, ranging from the wings of air-craft to air-conditioning heat exchangers. Frost layers formed through the frosting process decrease the working efficiency of heat exchangers and significantly increase electricity usage for defrosting. In order to delay frost processes, the rational design of anti-frost surfaces is necessary to increase the performance of heat exchangers and make them more environment-friendly. Anti-frost surfaces can employ the combination of surface chemistry modification and surface patterning containing micro or nanoscale features.

Here I reported an efficient method of preparing dealloyed porous copper with micro-nanoscale pores using copper-zinc alloy. The morphology of the porous copper is photographed by the scanning electron microscope (SEM), and the contact angles of the functionalized porous copper are measured by a contact angle meter. The frosting process on the porous copper samples is also studied using a customized set-up. The test results demonstrate different frosting behaviors on the porous copper samples with different

morphology and wettability. The fabrication method and test results may have implications for further nanoporous cupric materials design for anti-frosting and other thermal application.

# CHAPTER 1: Introduction

## 1.1. Conventional Anti-Frosting Methods

Frosting and icing processes are common phenomena in nature when water molecules are closely-arranged on cold surfaces from the moisture in the air. Frost and ice trouble people's lives. For example, ice and frost on roads, electric power lines, wings of airplanes, and fins of air-conditioning heat exchangers can decrease efficiency and induce damage for these devices and facilities, and even cause danger to human life. Through the history of human beings, people found ways to melt and remove frost and ice. Three traditional widely-used anti-frost or anti-ice methods include (1) mechanical removal, (2) surface heating, and (3) spreading salt.[1] However, mechanical removal is inefficient in time and cost. Heating the surface to melt ice and frost by the Joule effect is energy-consuming. Spreading salt is one of the chemical methods which is more efficient, but it corrodes roads and construction, and at the same time, the salt flushed into the soil and aqueous environment harms living species. Due to the current energy and environmental challenges, passive anti-frost or anti-icing methods using surface treatment are receiving more interest, which require different types of anti-frosting surface treatments.

## 1.2. Wettability

One promising anti-frosting surface treatment is to control the surface wettability by constructing rough features and manipulating surface chemical properties. The surface wettability is characterized by the static contact angle of water droplets on the designed surfaces, θ. As shown in Figure 1.1a, the contact angle of water droplets is only determined by the surface tensions of the three interfaces on a flat solid surface: the interfaces between the solid, liquid, and gas based on Young's equation, $\cos\theta = \frac{\gamma_{sv}-\gamma_{sl}}{\gamma_{lv}}$.[2] However, this model does not explain most of surfaces that contain rough features, defects, and impurities, requiring other models.

According to the Wenzel equation, $\cos\theta^* = r\cos\theta$ , the apparent contact angle $\theta^*$ of a surface is determined by the roughness, r, and the intrinsic contact angle, θ, and the roughness and the intrinsic contact angle further changes with the surface morphology and chemical properties, respectively.[3] As shown in Figure 1.1b, the Wenzel equation describes the state of a water droplet on a substrate without air pockets between the liquid and solid lines. For a surface with high roughness, the Wenzel equation does not fit because of the trapped air pockets in the rough structure under the water droplet. Cassie-Baxter equation, $\cos\theta^* = -1 + \emptyset_s(\cos\theta + 1)$, describes their contact angles, which relate to the solid area fraction of the substrate in contact with the liquid droplet, as illustrated in Figure 1.1c.[4]

To describe the liquid mobility and adhesion on a solid surface, the additional parameter of contact angle hysteresis Δθ is introduced, which is the difference between the advancing contact angle and the receding contact angle of the water droplet, as shown in Figure 1.1d. The smaller contact angle hysteresis explains droplet mobility on the surface.

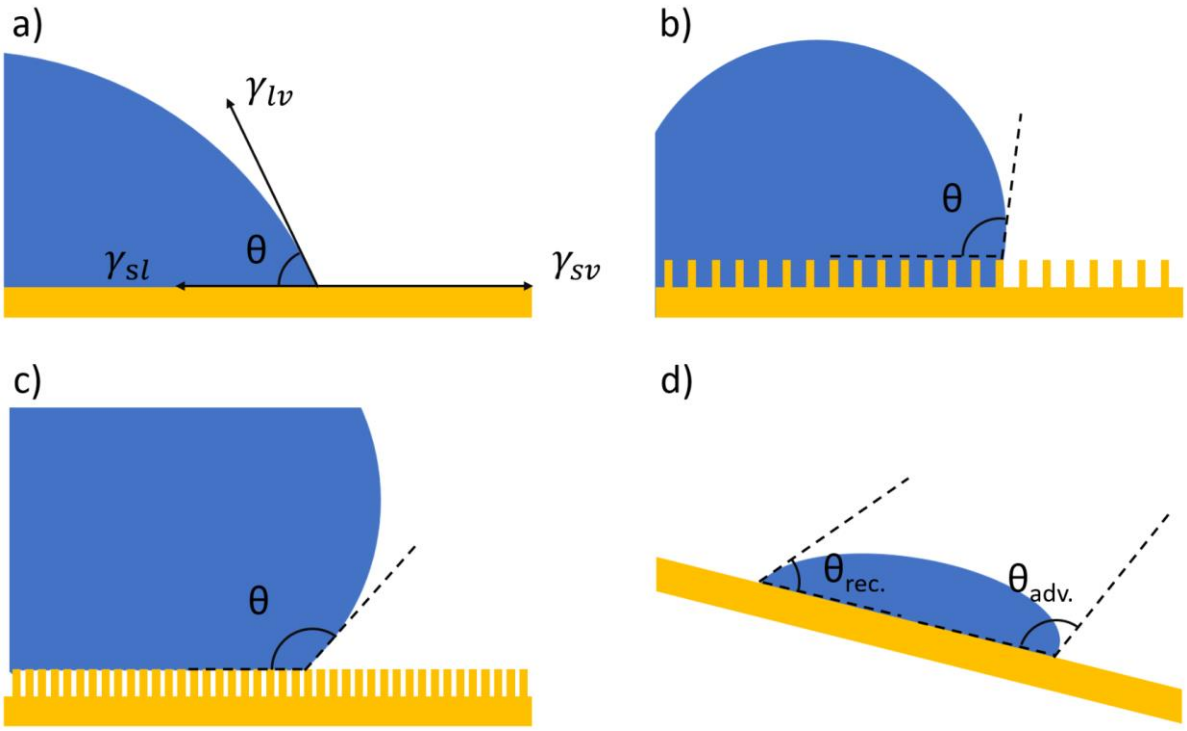


Figure 1.1 Schematic diagram of a water droplet (a) on flat surfaces showing solid-liquid, liquid-vapor, and vapor-solid contact lines. The illustrations explain the water droplets on rough surfaces explained by (b) the Wenzel state and (c) the Cassie-Baxter state. Dynamics wettability showing (d) the contact angle hysteresis that is the difference between advancing and receding contact angles.

According to the value of the static contact angle and the contact angle hysteresis of water, surfaces with different wettability can, therefore, be categorized. A surface with a contact angle lower than 90° is called as a hydrophilic surface, while one with a contact angle higher than 90° is called as a hydrophobic surface. Furthermore, the surface with a static contact angle higher than 150° and a contact angle hysteresis lower than 10° is superhydrophobic surface.

### 1.3. The anti-frosting performance of surfaces with different wettability

Although both hydrophilic surfaces and hydrophobic surfaces present anti-frosting abilities, they all face their problems that cause failure in anti-frosting. Heavy ice shells and frost melting water retention on the hydrophilic surfaces will harm the performance of devices working in a frosting environment.[5]–[8] Condensate droplets pinned on the hydrophobic surface with microstructures lack mobility and lead to film-wise condensation. Condensate water film freezing on a hydrophobic surface increases the weight of devices and declines the heat transfer rate from the surface. On a surface requiring highly efficient heat transfer and working in a frosting environment, people use surface treatment and fabricate it superhydrophobic to prevent film-wise condensation before freezing.[9]–[13]

Because of condensate droplet self-repelling and small liquid-solid interfaces, superhydrophobic surfaces are more efficient in anti-frosting than the hydrophilic and hydrophobic surfaces.[14]–[20] As shown in the equation, $\Delta P=\gamma\frac{2}{R}$ , Laplace pressure, the pressure difference that causes the curve surface between the gas region and liquid region, is determined by the surface tension between liquid and gas as well as the radii of curvature.[21] On a nano-structured superhydrophobic surface, a high Laplace pressure is available between the droplet and air pockets under it, which is attributed to the small radii coming with the nanoscale rough structures. Therefore, superhydrophobic surfaces with nanostructures are more robust against condensate droplet pinning, and condensate droplets can jump out of the surface by droplet coalescence. When a superhydrophobic surface is tilted or vertical to the ground, gravity will also help the self-removal of the

condensate water droplets. On the other hand, a spherical droplet in partial Cassie-state contacts the solid surface in a small area that contributes to low conduction heat transfer between the droplet and the surface. Since the superhydrophobicity introduces self-removal of condensate droplets before ice nucleation and freezing, the superhydrophobic surface presents stronger capability of delaying the droplets freezing and frosting.

### 1.4. Dealloying

To prepare the rough metallic structure for further functionalization and anti-frosting application, we select dealloying method. Among many techniques of fabricating rough porous metallic materials, the dealloying method is a facile one which is a process of solving the solvable metallic components in a multi-component alloy (with more than two components) and leaving the dissolvable components spontaneously forming bicontinuous porous structure. Figure 1.2 presents the porous structure reported previously and summarized by McCue and co-workers.[22] From our perspective, the dealloying method is promising in manufacturing porous metallic materials for three reasons: (1) dealloying is a template-less method to prepare a connective porous network, which avoids negative impacts caused by templates such as residual templates, limited scale, and high cost; (2)dealloying is relatively easy to conduct; (3) the pore size and porosity of dealloying metal can be controlled with parameters like the chemical composite of alloy and coarsening rate. Figure 1.3 illustrates the working model of dealloying process in the Au-Ag system. At the very beginning of dealloying, the less noble metallic atoms of the alloy solve into the solvent and are removed from the alloy matrix by an applied potential over the critical potential $V_C$.

Meanwhile, the sites where the less noble atoms used to occupy would be passivated by the nobler metallic components. Because of dissolving and passivation, the flat alloy surface turns rough. In the evolution of nanoporosity, the rate-limited step of dealloying the dissolution of the less noble metallic atom from the high-coordination sites. The nobler metallic atoms tend to gather into high-concentration areas from low-concentration areas which is an uphill diffusion. The uphill diffusion is helped by the rapid movement of more noble atoms in aqueous environments.

Then, with dealloying proceeding, noble metal atoms are not enough to passivate the freshly exposed surfaces efficiently which leads to the undercutting and bifurcation of pores. The nanopores grow through the alloy and a bicontinuous porous network forms.

Two parameters are identifying in dealloying: the parting limit $X_P$ and the critical potential $V_C$. The parting limit $X_P$ is the chemical composition of the less noble metal lower than which the dealloying cannot happen. The critical potential $V_C$ is a composition-dependent threshold parameter.[22]–[27] Oncethe applied electrochemical potential is over the critical potential, the ionic dissolution current is triggered.

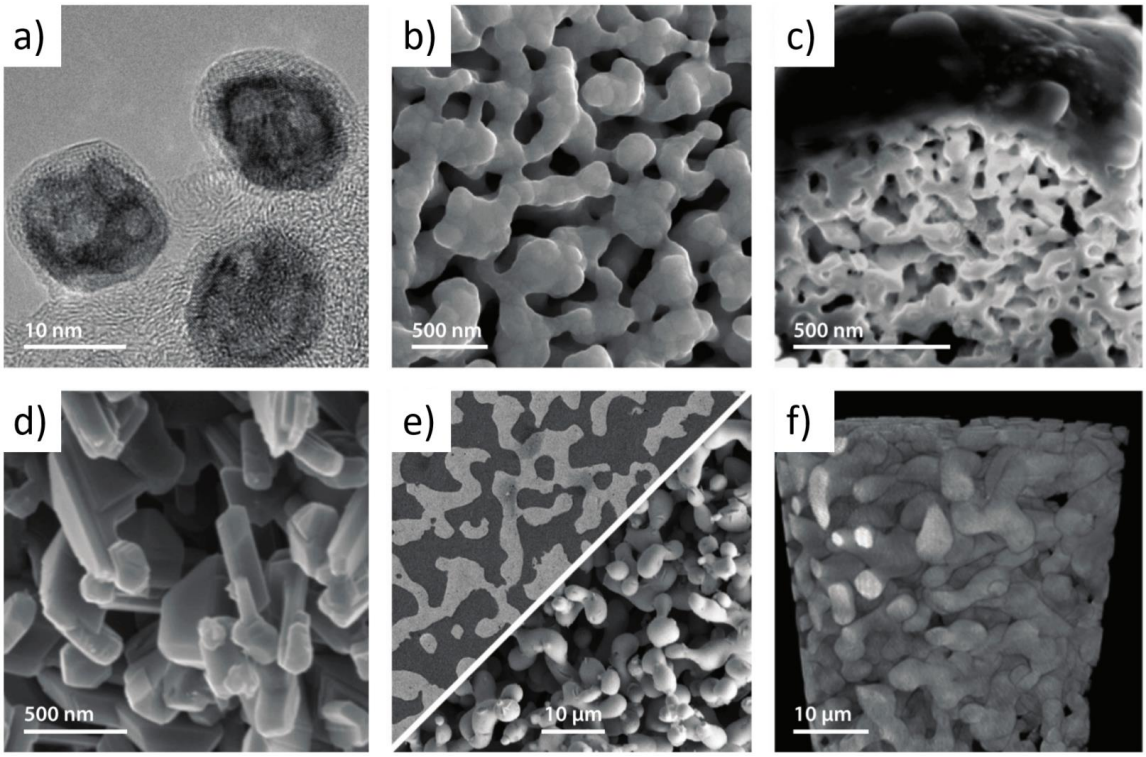


Figure 1.2 SEM Micrographs showing the porosity of dealloying materials**,** (a) nanoporous Pt, (b) nanoporous Au, (c) nanoporous Sn, (d) nanoporous Si, (e) nanoporous Ta, and (f) nanoporous Ti.[22]

Although the dissolution of less noble atoms occurs in molecular scale, nanoscale porous network tends to coarsen because of the large surface area exposed to the dealloying aqueous environments. In such aqueous environments, surface atoms are mobile enough to cause a bicontinuous pore size increasing with dealloying proceeding. In the dealloying process, the porous network is always coarsening. Coarsening decreases the surface area of the dealloying porous structure, but coarsening is a method to control the pore size. Because of coarsening, with the same alloy but for various dealloying times, one can fabricate dealloying porous network with a different pore size from nanoscale to microscale. [28]–[32]

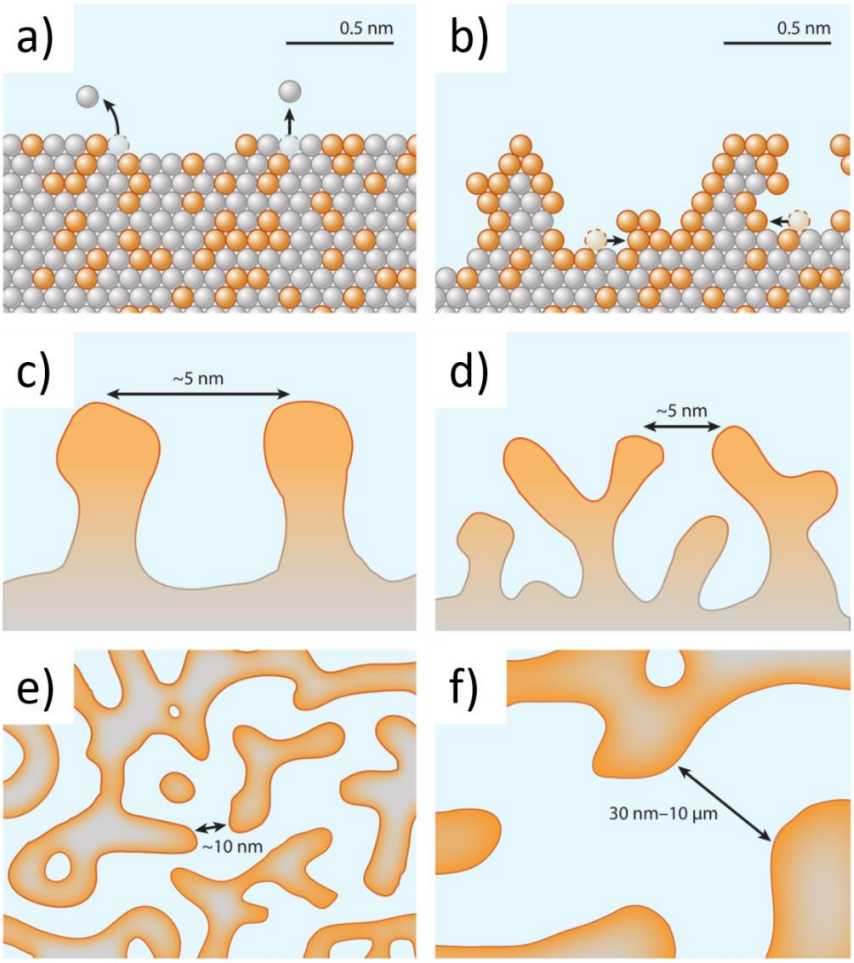


Figure 1.3 Schematic diagram of dealloying in the Ag-Au alloy system (Ag, gray; Au, orange) showing the atomic arrangement in the process of (a) the rate limiting step and (b) the surface roughening. The illustrations explain the porosity of dealloying materials after (c) undercutting, (d) bifurcation, (e) porosity evolution, and (f) coarsening. [22]

## 1.5. Object and Outline

In this thesis program, I aimed to realize anti-frosting on the surface of copper alloy by surface treatment: combining morphology construction and surface functionalization.

Copper is among the best conductors of electricity and heat and with outstanding ductility. Copper and copper alloys are widely used materials in the applications such as air-conditioning systems, architecture, manufacturing, electrical systems, renewable energy, seawater systems, pipe systems, and telecommunications. In working conditions that face frosting like in an air-conditioning and refrigerator heat exchanger, fabricating anti-frosting surfaces based on copper and copper alloy is promising to increase the heat exchanger efficiency, which is able to save considerable electricity, since 15% of energy consumption in human society spends on air-conditioning.

The thesis report includes the following aspects:

Chapter 1: Introduction

Chapter 2: Fabrication of Hierarchical Porous Copper Materials

Chapter 3: Characterization of Hierarchical Porous Copper Materials

Chapter 4: Anti-Frosting Measurement on Porous Copper

Chapter 5: Conclusions and Future Work

# CHAPTER 2: Fabrication of Hierarchical Porous Copper Materials

## 2.1. Introduction

Since the study of the dealloying porous gold was published in 2001[33], dealloying method has been focused on and explored as a promising method to manufacture continuous porous structure. The driving force and working model of dealloying metallic materials has been specifically introduced in **CHAPTER 1**.

Dealloying of brass is one of the earliest dealloying phenomena observed by human beings. Dealloying of brass was first learned as a kind of electrochemical corrosion. Dealloying is based on the different electrochemical potential of the different metal elements in the same electrolyte solution. As shown in Figure 2.1, the lowest potential for the copper cation to stay stable in the acidic aqueous environment is lower than that for the zinc cation, which means that there is an electrochemical potential window for the dissolution of zinc in the copper-zinc alloy. When the applied potential locates in the window, the current of the dissolution of zinc will rise over a low value that can be considered as the start of dealloying.

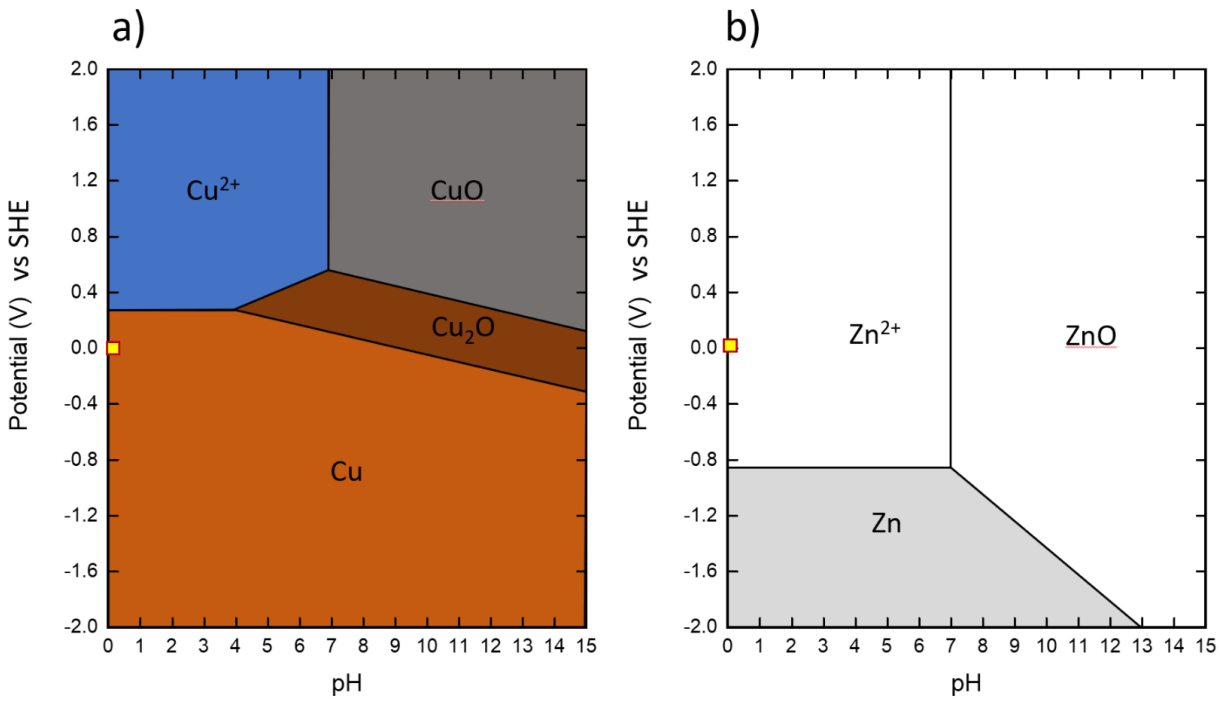


Figure 2.1 Schematic Pourbaix diagram of the (a) copper and (b) zinc.

In 2016, a chemical dealloying preparation method to fabricate porous copper using copper-zinc alloy has been published.[34] In that work, the authors reported that with a commercial bimetallic brass tape ($Cu_{64}Zn_{36}$), removal of zinc atoms leads to a continuous porous copper structure. The preparation of such porous copper structure can be achieved in an aqueous environment of 1 M HCl and 5 M $NH_4Cl$ solution at ~70°C for 12 hours. As the authors reported, the pore size distribution varies from 200 nm to 2 μm. The optical and SEM pictures are shown in Figure 2.2.

Although the dealloying method reported by the authors is simple and the fabricated porous network shows outstanding performance in the application of lithium-ion battery, the chemical dealloying is inefficient and time-consuming which requires 12 hours for dealloying a tape with thickness around 10 μm, and the pore size is distributed in microscale.

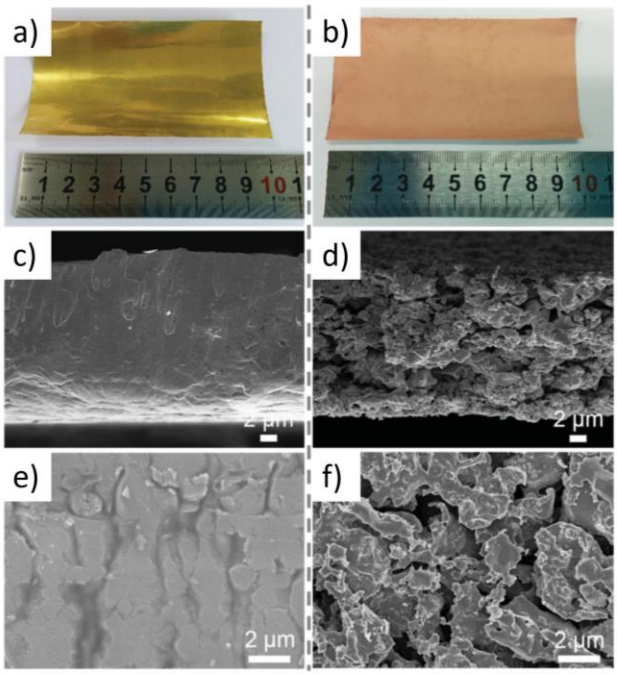


Figure 2.2 Morphology of the dealloying brass. Optical photos showing the brass (a) before and (b) after chemical dealloying. SEM images illustrating cross-section observation of brass (c) before and (d) after chemical dealloying, as well as top-view observation (e) before and (f) after chemical dealloying.[34]

In our opinion, the dealloying brass materials can be optimized in terms of two aspects: to make the dealloying process more efficient, and to make the structure finer and more ordered. With the help of electrochemistry, it is promising to make the dealloying brass process more efficient. Acid etching in low temperature or with pre-oxidation makes it possible to be finer and more ordered through hindering the diffusion rate of copper atoms. In the fabrication part, we explored the method of both electrochemical dealloying and acid etching. Compared to dealloying chemically, the method of electrochemical dealloying can be more controllable and more efficient.

## 2.2. Dealloying Brass by Electrochemical Corrosion

### 2.2.1. The electrochemical cell of dealloying

The electrochemical dealloying of the $Cu_{60}Zn_{40}$ alloy is performed in a three-electrode system. The set-up of the three-electrode set-up is shown in Figure 2.3. A Ag/AgCl (3M KCl) electrode is used as the reference electrode, and a carbon cloth electrode is used as the counter electrode. A brass bar (McMaster Carr) is used as the working electrode. A lid with holes is used to control the distance between the working, reference, and counter electrode. The distance between the working electrode and the reference electrode is set as 10 mm, and the distance between the counter electrode and the working electrode is set as 40 mm.

An aqueous solution of 1 M $NH_4Cl$ (Sigma-Aldrich) and 1 M HCl (Avantor Performance Materials). is used as the electrochemical dealloying electrolyte. The solution containing hydrochloric acid is diluted from the concentrated hydrochloric acid. The electrochemical cell is placed in a water bath in order to control the temperature of the electrolyte.

An electrochemical workstation (BioLogic SP-300) provides a consistent applied potential on the working electrode over a period of time. During the electrochemical dealloying reaction, the brass bar is used as the anode, and the carbon cloth is used as the cathode. The reaction happens on the anode is $Zn \rightarrow Zn^{2+} + 2e$. Those reactions that happen on the cathode are $2H^+ + 2e \rightarrow H_2 \uparrow$, and $2NH_4{}^+ + 2e \rightarrow H_2 \uparrow + 2NH_3 \uparrow$.

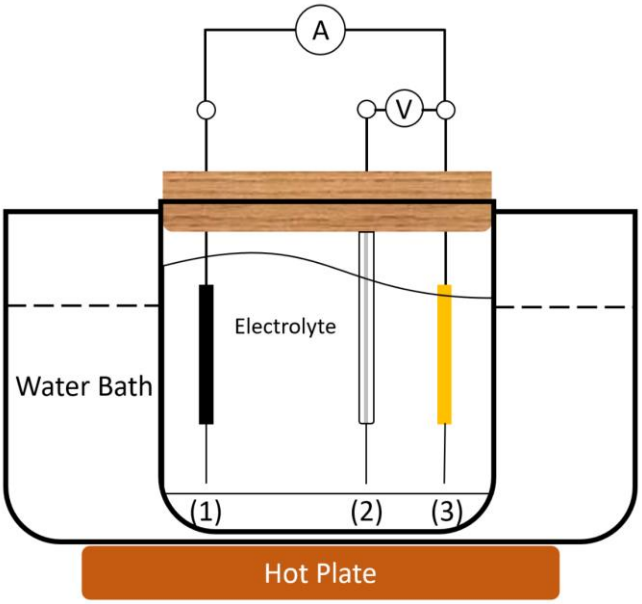


Figure 2.3 Schematic diagram of electrochemical cell design including the following components: (1) the counter electrode: carbon cloth, (2) the reference electrode: Ag/AgCl (3M KCl), and the (3) working electrode: $Cu_{60}Zn_{40}$ Alloy

### 2.2.2. Electrochemical dealloying parameter

Table 2.1 shows the parameters of electrochemical dealloying. With a constant applied dealloying potential, dealloyed brass for a various time at different temperatures has been studied. The dealloying temperatures are 20°C, 60°C, and 90°C. At 20°C, six pieces of brass bars with the size of 25 mm × 10 mm × 0.9 mm are dealloyed for 5 minutes, 10 minutes, 20 minutes, 40 minutes, 1 hour, and 5 hours. At 60°C and 90°C, set dealloying time decreases because of the increasing diffusion rates at higher temperatures.

Table 2.1Parameters of electrochemical corrosion.

| Potential | -0.2 V vs Reference electrode | | | | | |
|---|---|---|---|---|---|---|
| Temperature | Dealloying time | | | | | |
| Sample ID | EC01 | EC02 | EC03 | EC04 | EC05 | EC06 |
| 20°C | 5 min | 10 min | 20 min | 40 min | 1 hour | 5 hours |
| Sample ID | EC07 | EC08 | EC09 | EC10 | EC11 | EC12 |
| 60°C | 1 min | 3 min | 5 min | 10 min | 20 min | 1 hour |
| Sample ID | EC13 | EC14 | EC15 | EC16 | EC17 | |
| 90°C | 30 s | 1 min | 2 min | 4 min | 10 min | |

## 2.3. Dealloying Brass by Acid Etching

As for many other alloys, immersion in acid can process dealloying of brass as well. The $Cu_{60}Zn_{40}$ alloy is etched by diluted hydrochloric acid in this work. Pre-oxidation treatment has also been studied in this work. Table 2.2 presents the parameters of dealloying of brass by acid etching. For the etching of the bare brass, the molarity of the diluted hydrochloric acid varies from 1 M to 6 M. The temperature of acid etching is 5°C. The etching of the bare brass in acidic solution with different concentration maintains the same period of 24 hours. For the pre-oxidation of the brass, it takes 24 hours at 30°C. Pre-oxidized brass is etched with diluted hydrochloric acid for 5 minutes at room temperature.

Table 2.2 Parameters of Acid Etching.

| | | | | | |
|---|---|---|---|---|---|
| Acid Etching Bare Brass | Etching acid | HCl | | | |
| | Etching time | 24 hours | | | |
| | Temperature | 5°C | | | |
| | Sample ID | AE01 | AE02 | AE03 | AE04 |
| | Concentration | 1 M | 2 M | 3 M | 6 M |
| Acid Etching Pre-Oxidized Brass | Sample ID | AE05 | AE06 | | |
| | Pre-oxidation solution | 2 M NaOH | 2 M NaOH + 1 M $H_2O_2$ | | |
| | Pre-oxidation solution | 30°C | | | |
| | Pre-oxidation solution | 24 hours | | | |
| | Etching acid | 2 M HCl | | | |
| | Etching time | 5 minutes | | | |

## 2.4. Functionalization of Porous Copper

The functionalization of porous copper processes in a 5 mM ethanol solution of dodecanoic acid. After dealloying process, the porous copper is immersed in the 5 mM dodecanoic acid for 30 minutes and then dried in an air flow.

# CHAPTER 3: Characterization of Hierarchical Porous Copper Materials

## 3.1. Introduction

To characterize porous copper prepared by a dealloying method, we utilize the scanning electron microscope (SEM) to photograph the surface morphology of the porous copper samples. Using the contact angle meter, we measure the static contact angles of the functionalized porous copper samples. We further demonstrate the changes of surface morphology and contact angles with dealloying parameters.

Scanning electron microscope is an ideal instrument for characterizing the topography of the porous copper. The scale of the typical objects of scanning electron microscope locates at the range from tens of micrometers to tens observed in the nanometers. The pore sizes of the dealloying materials fit this range. Furthermore, scanning electron microscope have the advantage of a large depth of focus which is typically good at observing three-dimensional micro-nano structure. The scanning electron microscope photography is performed at the UC Irvine Materials Research Institute.

The contact angle measurement is performed at the Microscopic Contact Angle Meter (MCA-3 from Kyowa Interface Science). The contact angle meter is composed of three main parts: microinjector system, control boxes, and observation monitor. Through a capillary tip,

microdroplets with the volume of nanoliters can be dispensed on the surface of a sample by high-pressure air flow.

## 3.2. Porous Copper Fabricated via Electrochemical Corrosion

### 3.2.1. Morphological Details of Porous Copper Fabricated via Electrochemical Corrosion

Scanning electron microscopy (SEM) measurement of the morphology of the $Cu_{60}Zn_{40}$ alloy before and after dealloying treatment uses the FEI Quanta 3D FEG electron microscope. Figure 3.1 presents the surface morphology of $Cu_{60}Zn_{40}$ alloy before treatment. The surface of the purchased $Cu_{60}Zn_{40}$ alloy is smooth through the observation of both the SEM and Optical Microscope. No microstructure is observed through microscopy on the surface of the $Cu_{60}Zn_{40}$ alloy before surface treatment.

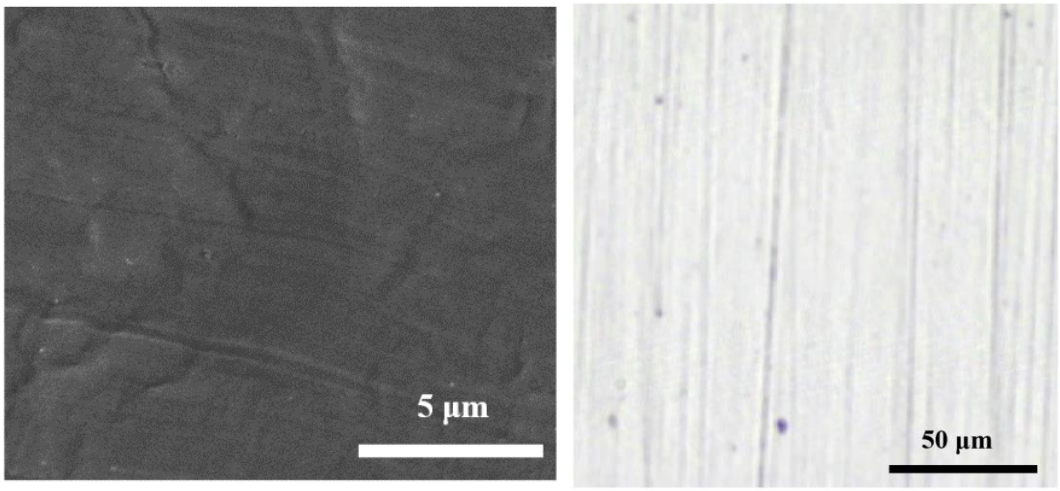


Figure 3.1 SEM picture and optical microscopy picture showing the surface morphology of the purchased $Cu_{60}Zn_{40}$ alloy

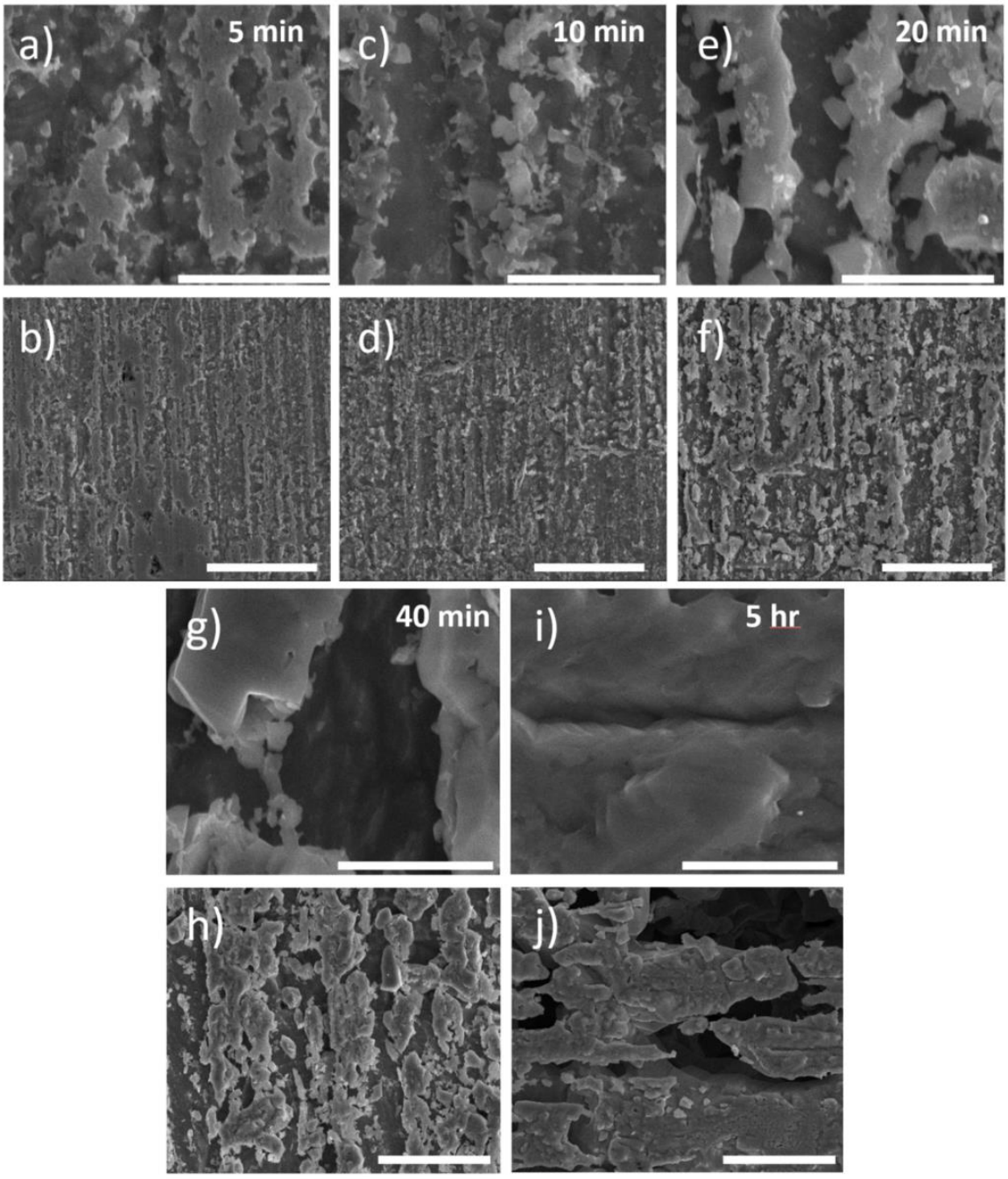


Figure 3.2 SEM pictures of the porous copper dealloying by electrochemical corrosion at 20°C showing the surface morphology of (a)(b) sample EC01, (c)(d) EC02, (e)(f) EC03, (g)(h) EC04, and (i)(j) EC06. Scale bars in (a)(c)(e)(g)(i) are 2 μm. Scale bars in (b)(d)(f)(h)(j) are 10 μm

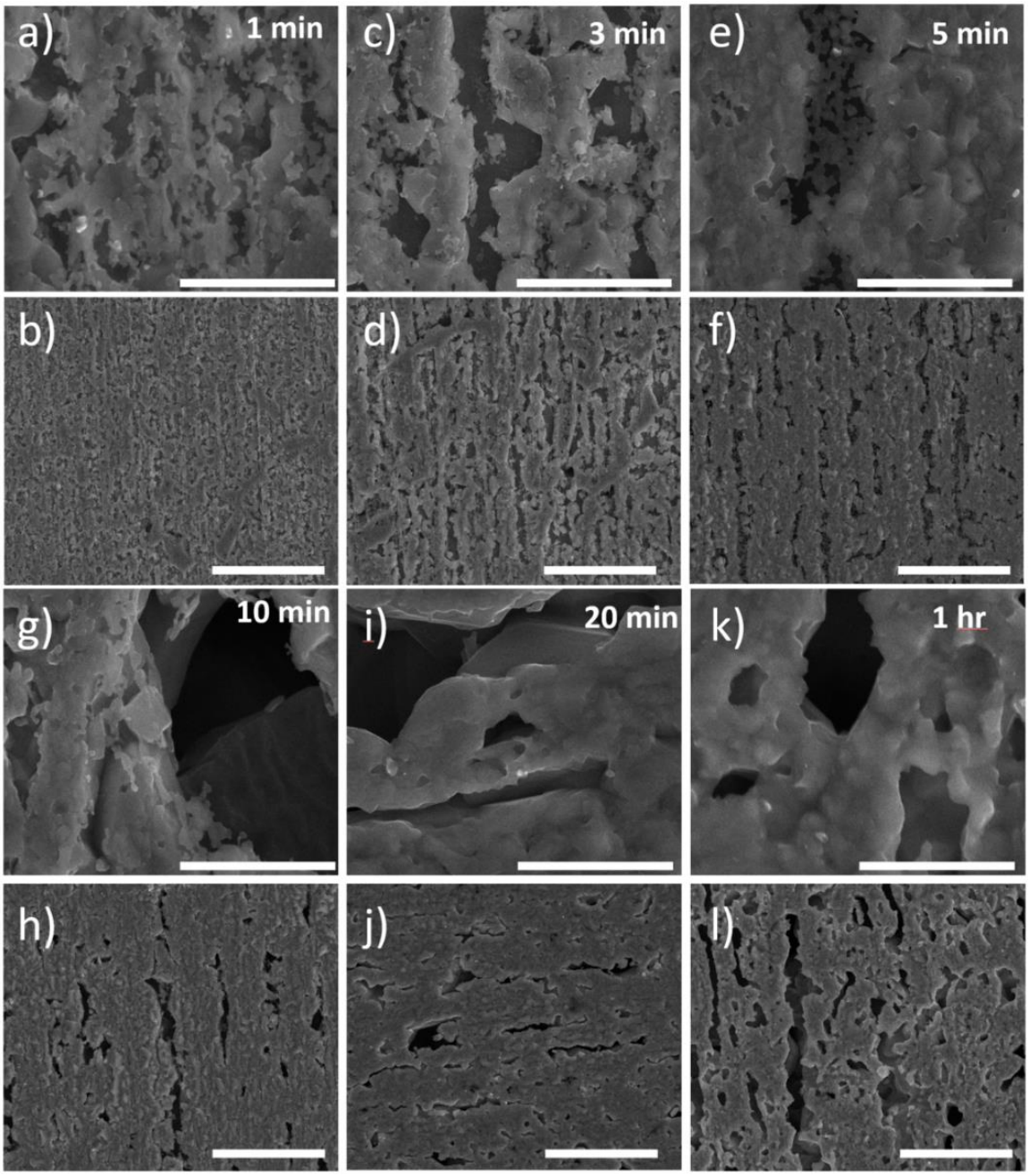


Figure 3.3 SEM pictures of the porous copper dealloying by electrochemical corrosion at 60°C showing the surface morphology of the (a)(b) sample EC07, (c)(d) EC08, (e)(f) EC09, (g)(h) EC10, (i)(j) EC11, and (k)(l) EC12. Scale bars in (a)(c)(e)(g)(i)(k) are 2 μm. Scale bars in (b)(d)(f)(h)(j)(l) are 10 μm

Figure 3.2 shows the surface morphology of porous copper dealloying at 20℃. The copper ridges form after the removal of zinc atoms. With the dealloying proceeding, the width of the copper ridges increases. When the alloy is electrochemically corroded for 5 hours (sample EC06), the hierarchical porous structure can be observed from the top-view SEM images. The formation of such hierarchical porous structure is attributed to the exhaustion of zinc atoms on the surface during dealloying. When the zinc atoms are depleted on the surface, electrochemical corrosion will happen between and beneath the copper ridges. Thereby, multiple layers of bicontinuous pore structure generate.

As shown in Figure 3.3, the copper worms structure generates as long as the electrochemical corrosion lasts for 1 minute. With the electrochemical corrosion proceeding, the copper worm structure is coarsening. This is caused by the diffusion of copper atoms. Compared with the surface morphology shown in Figure 1.2, the morphology of the $Cu_{60}Zn_{40}$ alloy dealloying at 60℃ is quite different on the density of pores. The pores in the top-view SEM images in Figure 3.3 are denser. The appearance of the multiple-layer pores is more rapid at a moment between 5 minutes (EC09) and 10 minutes (EC10).

Figure 3.4 presents the SEM pictures of the porous copper dealloying by electrochemical corrosion when the dealloying electrolyte is 90℃. When the alloy is dealloying for only thirty seconds, multiple-layer pores appear according to the SEM observation. With the increasing dealloying time, the pore size of dealloyed brass is growing which has been previously observed in the dealloying samples at 60℃. Due to the higher diffusion rate of copper atoms at the higher electrochemical corrosion temperature, the coarsening rate of the bicontinuous ridges and pores is higher for the samples corroded at 60℃.

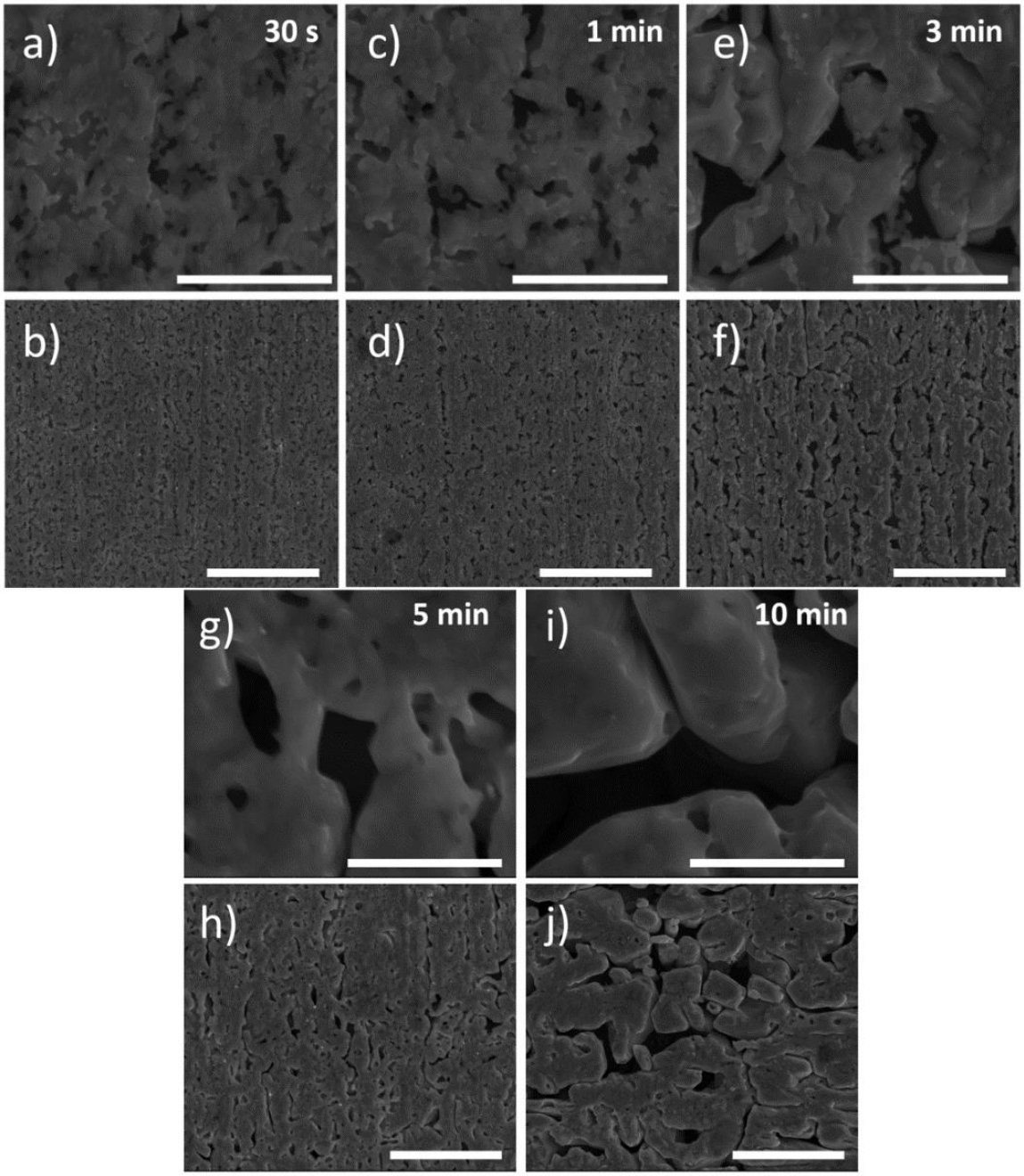


Figure 3.4 SEM pictures of the porous copper dealloyed by electrochemical corrosion at 90℃ showing the surface morphology of (a)(b) sample EC13, (c)(d) EC14, (e)(f) EC15, (g)(h) EC16, and (i)(j) EC17. Scale bars in (a)(c)(e)(g)(i) are 2 μm. Scale bars in (b)(d)(f)(h)(j) are 10 μm

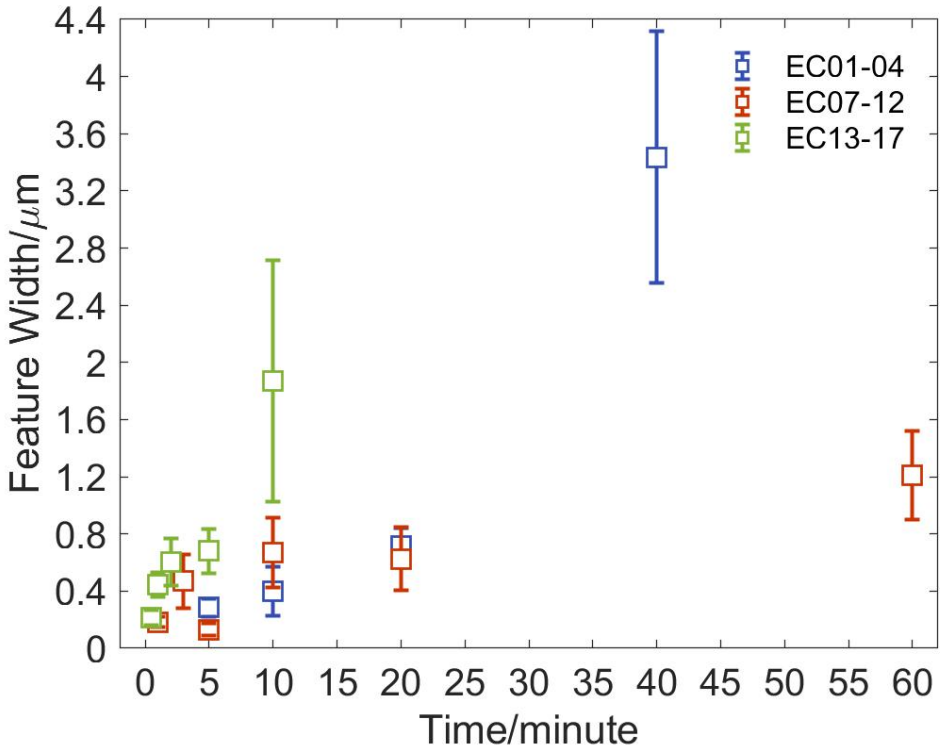


Figure 3.5 Feature width measurement of the porous copper dealloyed by electrochemical corrosion at 20℃ (EC01-04), 60℃ (EC07-12), and 90℃ (EC13-17).

The quantification of the feature width of the dealloyed $Cu_{60}Zn_{40}$ alloy samples is presented in Figure 3.5. The objects of the measurement are decided by the surface morphology of the samples. If the pores appear on the surface of the samples, the width of the pores are measured. The samples without pores are characterized based on the width of the ridges. Using the software Image J, we measured 10-14 points in two morphology images of each sample. Since the surface structure of the electrochemically corroded samples arranges in lines parallel, the feature width is measured through scaling the structure vertically to the arrangement direction.

### 3.2.2. Contact Angle Measurement of Porous Copper Fabricated via Electrochemical Corrosion

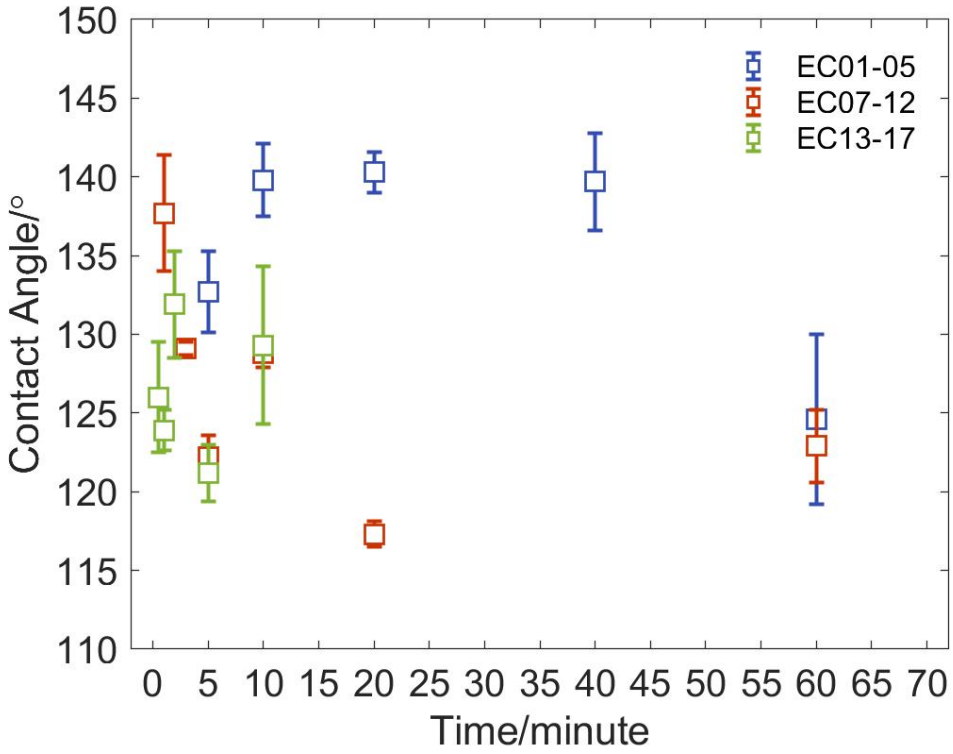


Figure 3.6 Contact angles of functionalized porous copper dealloyed by electrochemical corrosion at 20℃, 60℃, and 90℃ (Contact angles of sample EC01-05, EC07-17 are presented here. The contact angle of sample EC06 is 124.9 ± 4.7 with dealloying time as 5 hours is not plotted in this graph.)

Figure 3.6 presents the change of the static contact angle of the dealloying porous copper samples prepared by electrochemical corrosion with dealloying time. The plot of contact angles of the dealloying porous sample fabricated at 20℃ shows a platform from the dealloying time as 10 minutes to the time as 40 minutes (sample EC02-04). The contact angle value of this platform is around 140°. The peak value of this plot shows at 20 minutes

(sample EC03), which is 140.3°. According to the morphology study mentioned in the previous part, the increase of the contact angles of the 5-minute to 20-minute samples (EC02-03) is attributed to the appearance of the micro-ridges on the surface of brass, while the decrease of the contact angles of the 20-minute to 1-hour samples (EC03-05) is caused by the coarsening of the micro-ridges. The similar topography of the 10-minute, 20-minute and 40-minute samples (EC 02-05) leads to the platform of the contact angles.

The contact angle of the sample dealloyed at 60℃ (EC07-12) for a minute shows high contact angle as 137.7°. The high contact angle of such sample is because of the nano-ridge structure caused by electrochemical corrosion. However, the contact angles of the sample dealloyed at 60℃ tend to decrease because the structure of the porous copper fabricated by electrochemical corrosion is coarsening with the extension of time.

The contact angles of the samples electrochemically corroded at 90℃ (EC13-17) locate at the range from 120° to 135° which are caused by their nanoscale or microscale multiple-layer porous structure. Because of the difference in morphology between ridge-like structure and multiple-layer porous structure, the contact angles of the samples with structures in the similar sizes are quite different. For example, the sample corroded at 90℃ for a minute shows the multiple-layer nano-porous structure in the previous morphology study part, while the sample dealloyed electrochemically at 60℃ for a minute shows nano-ridge structures. Both of these two samples present nanoscale structure on their surfaces, but the contact angle of the nano-porous sample is 123.9° and the contact angle of the nano-ridge sample is 137.7°. There is a difference that is about 15°. Such difference of contact angle can also be found between microscale ridge-like surface structure and porous structure.

### 3.3. Porous Copper Fabricated via Acid Etching

#### 3.3.1. Morphological Details of Porous Copper Fabricated via Acid Etching

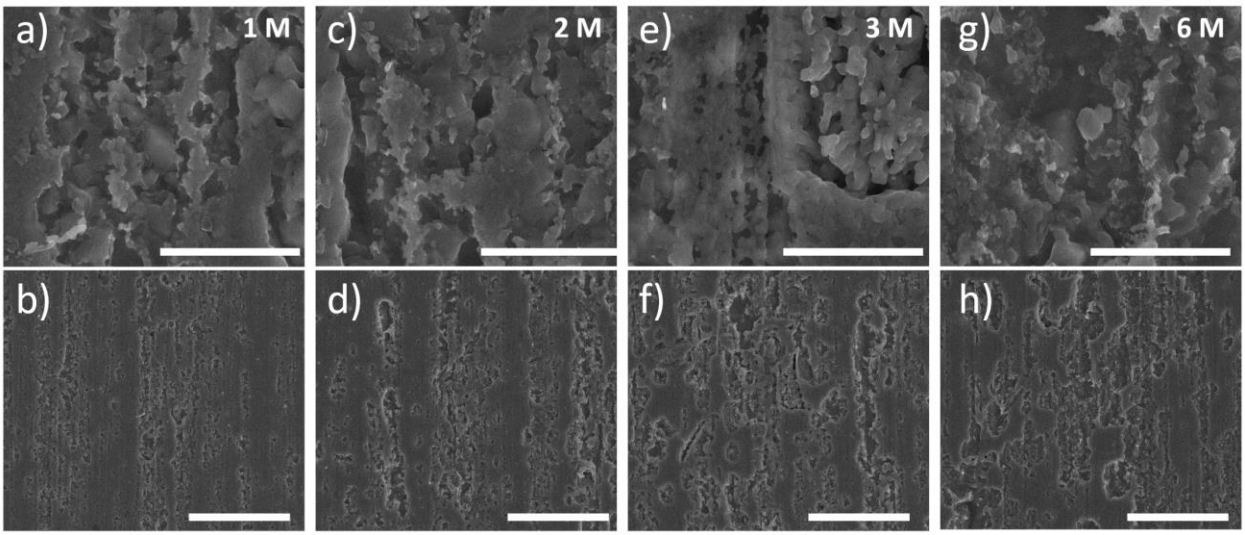


Figure 3.7 SEM pictures showing the surface morphology of bare brass dealloyed by acid etching at 5℃: (a)(b) Sample AE01, (c)(d) AE02, (e)(f) AE03, and (g)(h) AE04. Scale bars in (a)(c)(e)(g) are 2 μm. Scale bars in (b)(d)(f)(h) are 10 μm

Figure 3.7 presents the surface morphology of the $Cu_{60}Zn_{40}$ alloy etched in an acidic solution of HCl. When the concentration of HCl ranges from 1 M to 3 M (sample AE 01-03), the etching of alloy surface is increasingly severe. When the concentration of HCl approaches to 6 M (sample AE04), due to the dissolution of copper, the surface of the $Cu_{60}Zn_{40}$ alloy turns to be smoother. Compared with the samples fabricated through electrochemical corrosion, the samples prepared by acid etching do not present multiple-layer porous structure. Furthermore, this method of preparation shows lower efficiency than electrochemical corrosion.

The $Cu_{60}Zn_{40}$ alloy can be oxidized in an alkaline solution with an oxidant like oxygen or hydrogen peroxide. Due to the difference of electro-affinity between the copper and zinc atoms, the oxidation rates of copper atoms and zinc atoms through the depth of the sample are different. After the oxidation, the copper and zinc atoms will exist in the bulk of alloy as cations. Then, when the oxidized samples are put in an acidic solution like diluted hydrochloric acids solution, the metal oxide on the surface of alloy will dissolve. Since the zinc atoms are more oxidized during oxidation, more zinc cations than copper cations will dissolve during acid etching. Therefore, copper clusters with pores which were previously occupied by zinc atoms appear after acid etching.

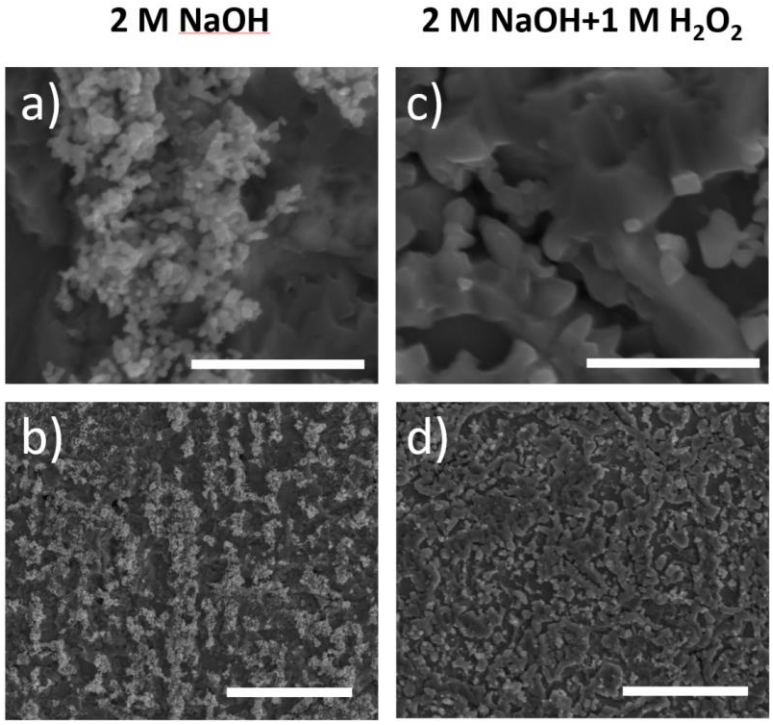


Figure 3.8 SEM pictures showing the surface morphology of the pre-oxidized brass dealloyed by acid etching: (a)(b) Sample AE05 and (c)(d) AE06. Scale bars in (a)(c) are 2 μm. Scale bars in (b)(d) are 10 μm

Figure 3.8 presents the surface morphology of the pre-oxidized brass after acid etching. The nanoscale porous structure is on the surface of the $Cu_{60}Zn_{40}$ alloy oxidized by the 1 M sodium hydroxide solution (AE05). For the samples oxidized by the mixture of 1 M sodium hydroxide and 1 M hydrogen peroxide (AE06), microscale ridge structure appears on the surface. Although there are rough structures on the surface of the pre-oxidized $Cu_{60}Zn_{40}$ alloy after acid etching, no bicontinuous porous structure shows in these samples.

The quantification of feature width of the acid etching samples is also presented in Figure 3.9. The feature width is measured through the software Image J. 10-14 points in two images of each sample have been measured to decide the feature width.

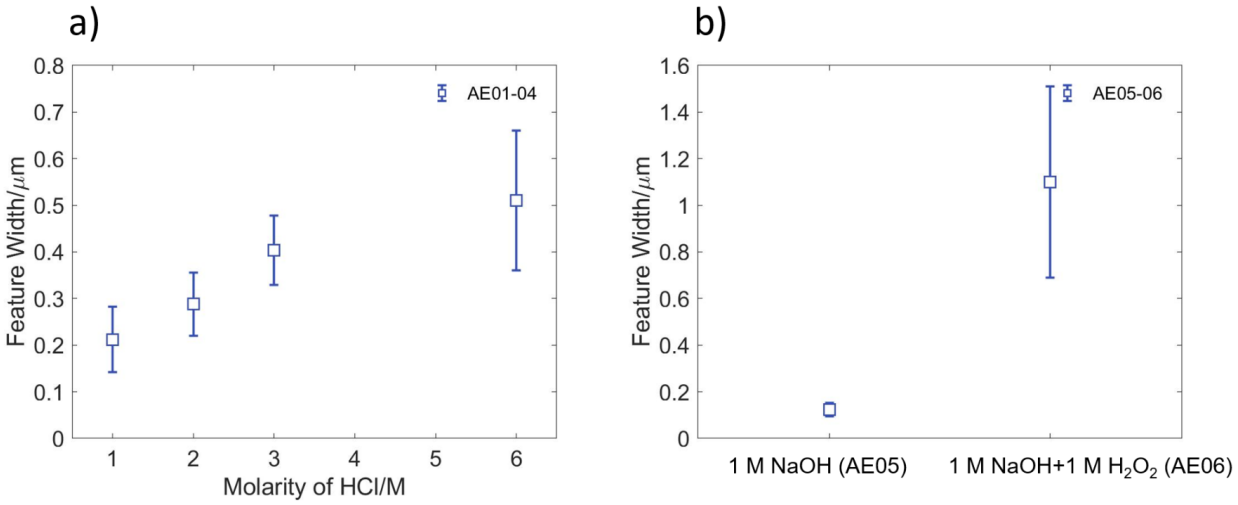


Figure 3.9 Feature width measurement of functionalized porous copper dealloyed by acid etching (a) without pre-oxidation (AE01-04) and (b) with pre-oxidation (AE05-06)

### 3.3.2. Contact Angle Measurement of Porous Copper Fabricated via Acid Ecthing

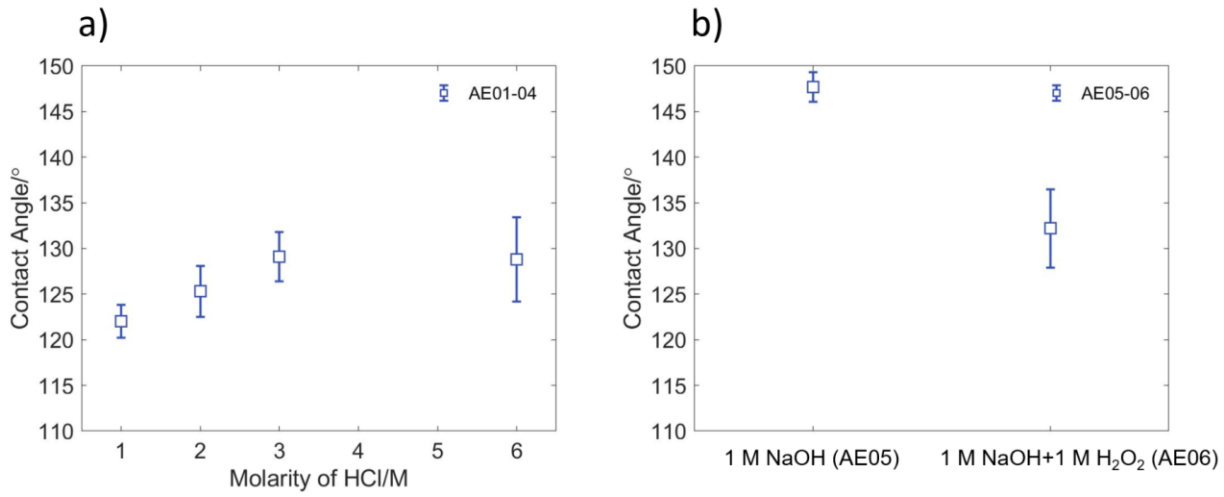


Figure 3.10 Contact angles of functionalized porous copper dealloyed by acid etching (a) without pre-oxidation (AE01-04) and (b) with pre-oxidation (AE05-06)

The contact angle measurement results of functionalized porous copper dealloyed by acid etching without pre-oxidation (AE01-04) are plotted in Figure 3.10a. The contact angles of acid etching samples increase with molarity increasing when the molarity of HCl ranges from 1 M to 3 M (AE01-03). The contact angle climbing with increasing molarity of HCl stops when the molarity of HCl is 6 M (AE04) which matches with the morphology characterization. The contact angles of functionalized porous copper dealloyed by acid etching with pre-oxidation (AE05-06) are shown in Figure 3.10b. Because of the clusters of copper nano-structure, the contact angle of the dealloying sample pre-oxidized by the solution of sodium hydroxide (AE05) is as high as 147.7°. Due to the micro-structure presented in the topography study, the contact angle of the dealloying sample pre-oxidized by the solution of sodium hydroxide and hydrogen peroxide (AE06) reaches 132.2°.

## 3.4. Comparison between Porous Copper Fabricated via Electrochemical Corrosion and Acid Etching

Compared to dealloying method via acid etching, dealloying through electrochemical corrosion is more efficient. According to the morphology characterization of dealloying sample via electrochemical corrosion, the bicontinuous porous structure on the surface appears after dealloying for 5 minutes at 60℃ (EC09) and dealloying for 30 seconds at 90℃ (EC13). In comparison with the fast fabrication of bicontinuous porous structure in micro-nanoscale, the process of acid etching with or without pre-oxidation takes at least 24 hours, but no bicontinous porous structure appears on all six samples (AE01-06). Although clusters of nanostructure appear on the surface of acid etching sample pre-oxidized by sodium hydroxide (AE05), the aggregation of nanostructure and uniformity of the surface indicates such sample is not perfect for real-world application. Since samples prepared via electrochemical corrosion show advantage in high fabrication efficiency and predictable morphology, we select the samples fabricated via electrochemical corrosion for further frosting behavior study.

## 3.5. Conclusion

In this chapter, we have investigated the effects of dealloying process parameters on the morphology and wettability of the porous copper samples. On one hand, through both electrochemical corrosion and acid etching method, dealloyed samples with ridge-like structures and multiple-layer porous structures are fabricated, and the morphology is

recorded using SEM. We have demonstrated that dealloying time and dealloying temperature through electrochemical corrosion method has a significant impact on the surface morphology of the dealloying samples. On the other hand, we have measured the contact angles of the functionalized dealloying porous copper samples through electrochemical corrosion and has found that the contact angles are related to the surface morphology and its longitudinal scale.

# CHAPTER 4: Anti-Frosting Measurement on Porous Copper

## 4.1. Introduction

To test the potential of the dealloyed porous copper in the anti-frosting application, anti-frosting measurement of these prepared porous copper is conducted and reported in this chapter. This chapter includes the following four parts: the set-up of anti-frosting measurement, the frosting model on a cold surface, the frost growth on porous copper and the conclusions.

The frosting is a heterogeneous process of water vapor deposition on the chilled solid surfaces. The morphology of the solid surfaces has an obvious impact on the frosting process. In this chapter, the frosting behaviors of the dealloyed samples with three different topography are studied.

The changes of the frost height with time is an important parameter to quantify the frosting process on cold surfaces. In the frost growth on porous copper, the changes of frost height with time have been recorded and measured.

## 4.2. Set-up of Anti-Frosting Measurement

The frosting performance on porous coppers is observed through a set-up designed and built by us as shown in Figure 4.1. The set-up is made up of five main parts: the humidity and temperature measurement system, the cooling system, the humidity supply system, the optical microscope, and the environment chamber.

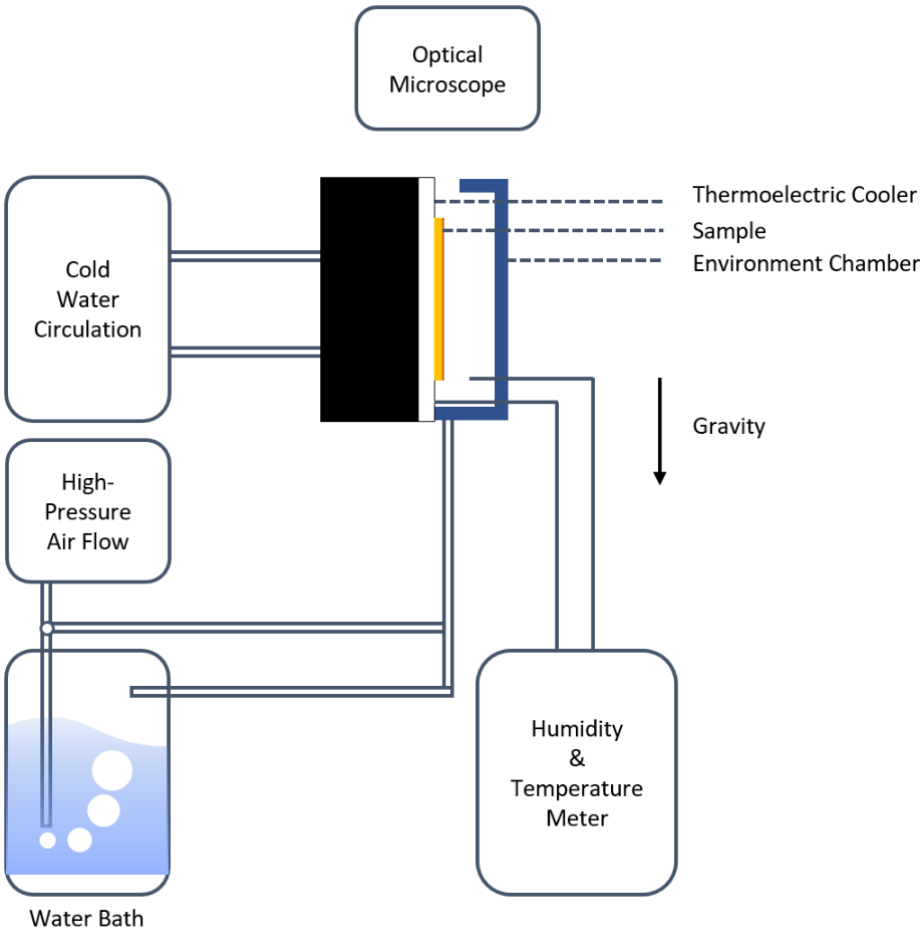


Figure 4.1 Schematic diagram of frosting test set-up showing the set-up is made up of five components: the cooling system (cold-water circulation, sample stage and the thermoelectric cooler), the temperature and humidity measurement system, the humidity supply system (the high-pressure air flow and the water bath), the optical microscope and the environment chamber.

The cooling system includes a cold-water circulation, a custom-made metal sample stage and a thermoelectric cooling module. The custom-made metal sample stage is connected in the cold-water circulation, and the thermoelectric cooling module is further fixed on the metal

sample stage. A DC power source is used to supply electric potential on the ends of the thermoelectric module. Because of the cooling system, the temperature of the sample can drop down to - 18℃.

The humidity and temperature measurement system are composed of a thermo-hygrometer and a temperature meter. The thermo-hygrometer is purchased from Hanna Instruments with the measurement range of relative humidity from 20 % to 95 % and accuracy as ± 5%. The temperature meter is purchased from Omega. The probe of humidity meter is inserted in the center of the environment chamber to detect the humidity in the chamber. The thermocouple is fixed between the sample and the thermoelectric cooler module. The temperature of the sample is monitored by the temperature meter.

The humidity supply is realized by leading a high-pressure air flow through a water bath. The air flow goes out of the water bath is with relative humidity close to 100%. A three-way valve is set in the tube before the high-pressure air flow goes through the water bath. Therefore, the dry high-pressure air flow can go directly to the environment chamber. Adjustment of the switch and the original pressure of the air flow can manipulate the relative humidity inside the environment chamber.

The environment chamber is designed in SolidWorks and printed out by an AirWolf 3D printer. The diameter of the environment chamber is 40 mm × 40 mm × 35 mm. With the two tubes on the front and back side of the cubic chamber, the humidity-supply air flow can go through the chamber and provide the humidity for frosting measurement. A custom-made optical microscope is used for observation of the frosting process. As shown in the optical picture of the bare brass before surface treatment, the resolution of the optical microscope

can reach several micrometers. The frosting process is recorded and analyzed in the situation: the temperature of the sample is – 3 ± 0.5℃, and the relative humidity in the chamber is 85 ±5%

### 4.3. Frosting Model on Cold Surface

The frosting process has been recorded which can be concluded as the following model. According to observation, the frosting process on the cold surface includes three processes: condensation, icing, and frost growth, as shown in Figure 4.2.

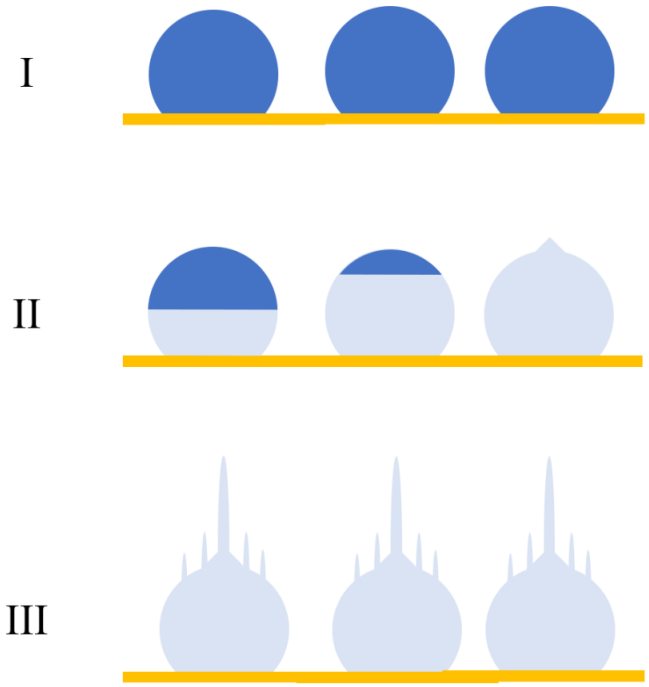


Figure 4.2 Schematic diagram of frosting process observed from the side-view on flat surfaces showing three different periods of frosting: (I) Condensation, (II) Icing, and (III) Frost growth

At the beginning of the condensation period, the water droplets nucleate on the cold surface. The condensate droplets grow up in this period through both condensation and droplets coalescence. As the condensate droplets pinned on the cold surface, through the conductive heat transfer from the droplets to the cold surface, the temperature of the droplets will decrease which leads to the freezing of the condensate droplets on the cold surface.

As shown in Figure 4.2, the icing process starts at the bottom of a droplet where is the interface between the liquid phase and the solid phase. Observed from the side view, the condensate droplets froze one by one along one direction like dominoes. Figure 4.3 presents optical micrographs of the icing process for a single condensate droplet. The icing process is rapid and completed in 3 seconds. During the icing of the single condensate droplet, an interface between the water and the ice can be clearly observed. Above the interface is water, while under the interface is the ice. Such interface raises from the bottom to the top of the droplet. When the interface arrives at the top of a droplet, the icing process is completed. Due to the expanding of the droplet during freezing, a sharp cone will leave at the top of the frozen droplet.

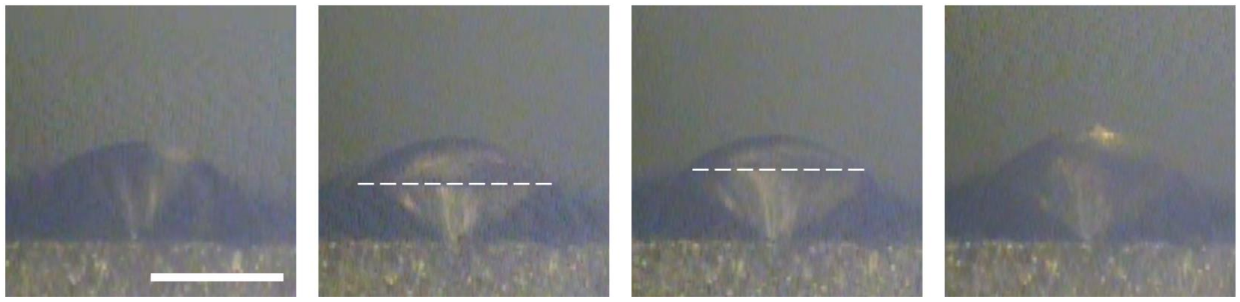


Figure 4.3 Optical microscope pictures of icing process on a flat brass surface. The length of the scale bar is 0.4 mm.

The third period of frosting is the frost growth. After droplets freezing, frost crystals are prior to grow at the top cone of a frozen droplet, because the radius of curvature of the top cone is smaller. According to a theoretical modeling of focused diffusion and heat flux on the apex of spherical-cap-shaped bumps using a spherical mass sink and source geometry reported by Kyoo-Chul Park and etc. [35], both diffusion and heat flux is proportional to the reciprocal of the radius of curvature. $J_c \sim \left.\frac{dC}{dh}\right|_{h\to 0} \sim \frac{1}{\kappa^{-1}}$. $J_T \sim \left.\frac{dT}{dh}\right|_{h\to 0} \sim \frac{1}{\kappa^{-1}}$. $J_C$ and $J_T$ are respectively the diffusion flux and heat flux. $\kappa^{-1}$is the radius of curvature.

Because of both larger local heat and diffusion flux on the top cone of the frozen droplet, frost crystals will grow outward the sample surface and form frost array on the surface. Along with the growth of the frost array, the temperature of the top of frost crystals is damping. Then, the water vapor tends to condensate in the pores and gaps of the frost array.

### 4.4. Frost Growth on Porous Copper

To observe the frost growth on porous copper, porous copper samples with three different topographies are picked for the frosting test: EC04, EC07 and EC14. As mentioned in the previous fabrication section, sample EC04 is prepared by electrochemical corrosion at 20°C for 40 minutes; sample EC07 is electrochemically corroded at 60°C for a minute; sample EC14 is dealloyed at 90°C for a minute through electrochemical corrosion method. The morphology of these three samples are also presented in the previous materials characterization section. The fabrication parameters and properties of the tested samples are listed in Table 4.1. A brass before surface treatment is measured for reference as well.

Table 4.1 Parameters of frosting test samples

| Sample ID | Dealloying Temperature (℃) | Dealloying Time (min) | Feature Width (μm) | Contact Angle |
|---|---|---|---|---|
| EC04 | 20 | 40 | 3.44 | 139.7° |
| EC07 | 60 | 1 | 0.18 | 137.7° |
| EC14 | 90 | 1 | 0.44 | 123.9° |

The frosting tests of these three porous copper samples are performed in the situation mentioned previously. The frosting process of the porous copper is recorded by the microscope, and the droplets and frost in the recorded video are further measured using Image J. One image is saved per two minutes in the one-hour video. For every image, ten to seventeen points are measured and averaged to determine the height of water droplet or frost at that moment.

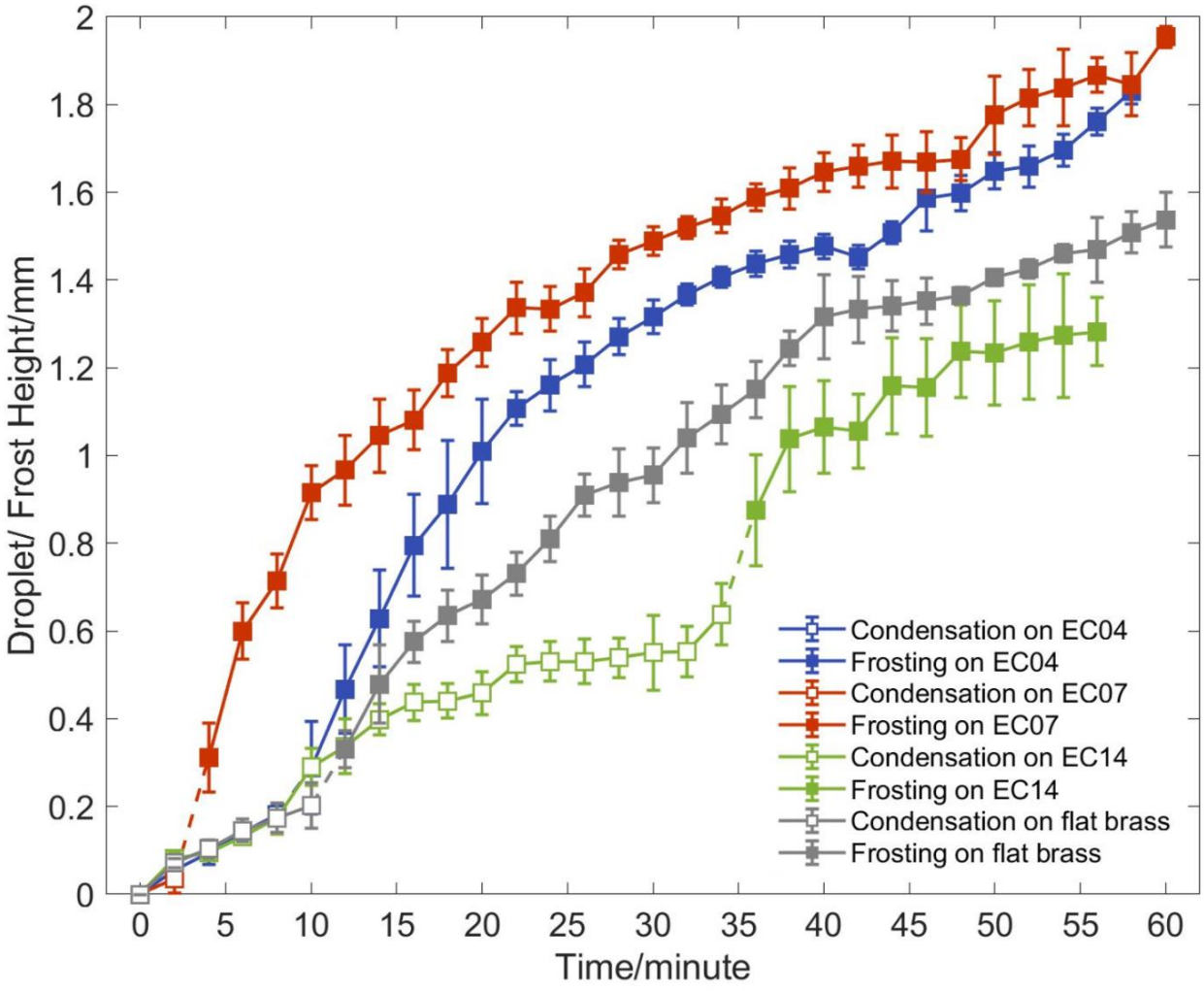


Figure 4.4 Diagram of the change of droplet/ frost height with time of sample EC04, EC07, EC14 and a flat brass sample

Figure 4.4 presents the droplet/ frost height changes with time of sample EC04, EC07 and EC14. Figure 4.5 shows the optical microscope pictures of a different period in the frosting process on three dealloyed sample as well. With regard to the condensation period, all three samples show similar growth rate in terms of the height of droplets. From our perspective, the similar droplet height growth rate can be justified by two reasons. One reason is that the

condensate droplets grow in spherical shapes which makes the increasing value of droplet height is relatively small because the increasing amount of the droplet height is only the cubic root of the volume of condensate water. The other reason is that the state of the condensate water droplets on these three surfaces are the same: the droplets are all in the Wenzel state on hydrophobic surfaces. Due to the state of the droplets on the surfaces, they are growing through nucleation, water vapor condensation from the environment, and the coalescence of water droplets. No droplet self-jumping phenomenon has been observed on the surfaces. Therefore, no scatter in droplet height shows in the plots. Because of the hydrophobicity of the surfaces, the droplets keep growing in dropwise condensation instead of film-wise condensation before freezing.

Figure 4.5 shows the optical microscope pictures of the droplet after freezing on three different surfaces. The icing period of the sample EC04, EC07 and EC14 starts before 10, 4, and 36 minutes, respectively. The surface morphology shows significant impacts on the frosting delay. The frosting delay of the sample EC04 and EC07 is obviously shorter than the sample EC14. We think such phenomenon is caused by the convex structures on the sample EC04 and the sample EC07 which provide sufficient nucleate points for nucleation and decrease the Gibbs free energy barrier required for phase transformation. The frosting delay of sample EC07 is shorter than the sample EC04 because the nanoscale structure is denser to boost icing on the surface.

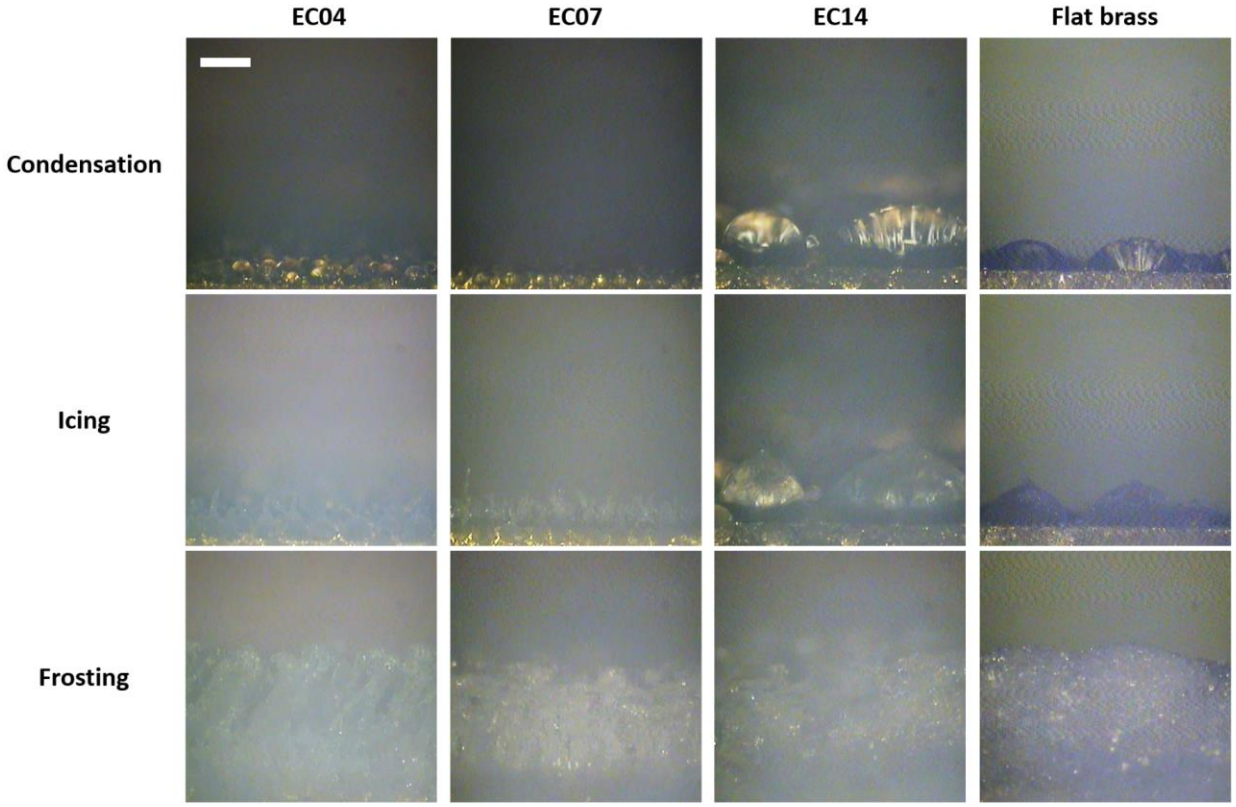


Figure 4.5 Optical microscope pictures of frosting process on porous copper sample EC04, EC07, EC14 and a flat brass sample. The length of the scale bar is 0.4 mm.

Figure 4.5 shows the optical microscope pictures of the droplet after freezing on three different surfaces. The icing period of the sample EC04, EC07 and EC14 starts before 10, 4, and 36 minutes, respectively. The surface morphology shows significant impacts on the frosting delay. The frosting delay of the sample EC04 and EC07 is obviously shorter than the sample EC14. We think such phenomenon is caused by the convex structures on the sample EC04 and the sample EC07 which provide sufficient nucleate points for nucleation and decrease the Gibbs free energy barrier required for phase transformation. The frosting delay of sample EC07 is shorter than the sample EC04 because the nanoscale structure is denser

to boost icing on the surface. Compared to the sample EC04 and EC07, the sample EC14 has nanoscale pores located on one plane. Such nano-pores can not only provide re-entrant structures that trap air pockets under the water phase but also avoid boosting icing by providing geometric nucleation point.

In the frost height plots of all the three samples shown in Figure 4.4, rapid rises of frost growth rate appear right after droplets freezing. The rise is attributed to the frost crystal growth on the cone of the frozen droplet as shown in Figure 4.5. The frost crystal growth along with the cone also causes a big difference of height between the center of frozen droplets and other points on the surfaces. Therefore, large errors are observed in the plots with the rapid increases of the frost height.

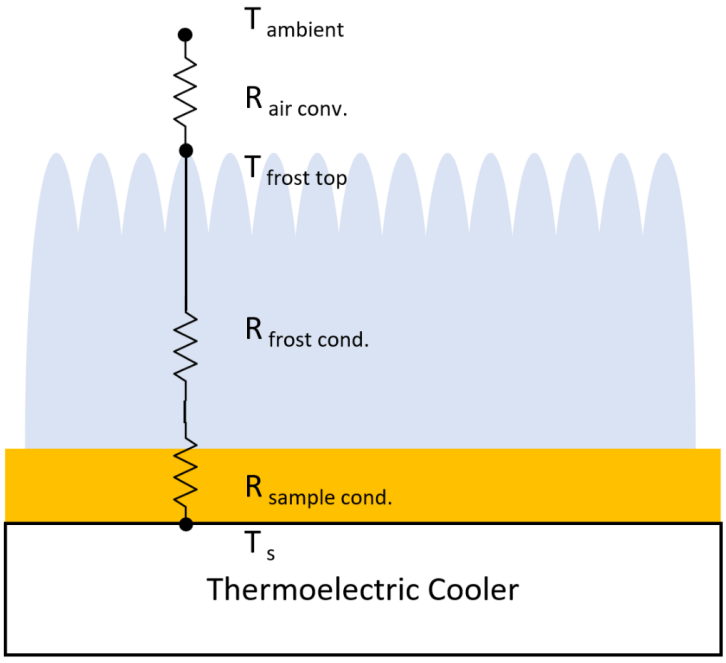


Figure 4.6 Schematic diagram of the thermal resistance circuit in the frosting test showing the frost arrays on a porous copper sample attached to a thermoelectric cooler

After icing process, the frosting on the cold porous surfaces is in the frost growth period. The plots of all the three samples show that frost growth is slowing down with time and tend to stop eventually. The decrease of frost growth rate is led by the increase of the thermal resistance of the frost layer. As shown in Figure 4.6, the temperatures of the sample $T_S$ and the ambient temperature $T_{ambient}$ are fixed. As measured, the temperature difference between the bottom and the top of the sample during testing condition is close to 0.1℃ that is comparable to the accuracy of the measurement system. The thermal resistance of the sample, $R_{sample\ cond.}$ is small enough to be ignored.

Therefore, the temperature of the frost top surface $T_{frost\ top}$ is decided by the convective thermal resistance, $R_{air\ conv.}$ and the conductive thermal resistance of frost layer, $R_{frost\ cond}$. $R_{air\ conv.}$ is the reciprocal of the heat transfer coefficient, h times the frost surface area, A. With the increase of the thickness of frost layer, h can be considered as the same and the surface of frost array increases leading to the decrease of $R_{air\ conv.}$ $R_{frost\ cond}$. in the experiments increases with the thickness of the frost layer. Therefore, with the frost height increasing, $T_{frost\ top}$ is increasing. The increasing $T_{frost\ top}$ leads to less temperature difference that is the driving force of frosting. Furthermore, droplets will start condensation on the top of frost layer when the frost layer is thick enough, and the condensate droplets will freeze on the top of frost layer as well. The plots of the sample EC04 and sample EC07 in Figure 4.4 present ballooning of errors when the frost height is over 1.6 mm which is attributed to the icing of condensate droplets on the top of frost layer.

## 4.5. Conclusion

In this chapter, we have investigated the frosting process on the porous copper samples with three different surface morphologies: EC04, EC07 and EC14. First of all, we designed and built a frosting experiment setup to manipulate the temperature and relative humidity for frosting experiment. Secondly, we have demonstrated the frosting process on the cold porous copper surfaces. We categorized the frosting behaviors on the porous copper surfaces into three different types: condensation, icing and frost growth. Finally, we measured two important parameters of the frosting process on the surface of dealloying samples, frost height, and frosting delay. We have demonstrated that surface morphology of the dealloying samples affects the frost height and frosting delay. In terms of these two parameters, the sample EC14 is better than the other two samples.

# CHAPTER 5: Conclusions and Future Work

In this work, we have explored both chemical and electrochemical methods to fabricate porous dealloying copper materials using the $Cu_{60}Zn_{40}$ alloy. One motivation of this thesis is to find an efficient method to fabricate bicontinuous structure through the process of dealloying. Compared to the chemical method, acid etching, the dealloying method through electrochemical corrosion is more efficient in preparing porous structure on the surface of brass. We have investigated the surface morphology of dealloying copper which is influenced by the dealloying parameters like dealloying time and dealloying temperature. Increasing dealloying time will cause the coarsening of surface structures of dealloyed copper while higher dealloying temperature leads to finer porous structure and faster evolution of the topography. Through controlling the dealloying time and temperature in electrochemical corrosion, ridge-like and porous surface structures with width ranging from hundreds of nanometers and several micrometers have been possible. By measuring the contact angles of the electrochemical corroded samples, we demonstrated the relationship between the wettability of the samples with the surface morphology.

After successfully preparing dealloying copper samples with different morphologies, we selected samples with three different morphologies to study the impact of surface morphology on the frosting behaviors, which are the Micro-Ridge, the Nano-Ridge and the Nano-Pore structures. We focused on two important parameters of the frosting process, the frost height changes with time and the frosting delay. In terms of these two parameters, the Nano-Pore sample presents the best performance as forming 1.6-mm frost layer for one-hour test and delaying frosting for 36 minutes.

However, some limitations exist in this work, and further research can be conducted in the future. In this work, the purchased $Cu_{60}Zn_{40}$ alloy is used for dealloying study, whose composition of copper is high and fixed. The high composition of copper limits the porosity of dealloying porous copper. If an alloying process can be included to prepare composition-designed alloys, the dealloying of the brass with the copper-zinc atomic ratio lower than 30:70 or the three-component brass will be possible. Through this method, the porosity and pore size presented in this work can be further improved for heat and mass transfer application. Furthermore, we will also measure and quantify the frosting behavior of the remaining porous copper samples and explore the fundamentals of the frosting behaviors we observed.

## REFERENCE


[1] J. Lv, Y. Song, L. Jiang, and J. Wang, "Bio-Inspired Strategies for Anti-Icing," *ACS Nano*, vol. 8, no. 4, pp. 3152–3169, Apr. 2014.

[2] H. J. Cho, D. J. Preston, Y. Zhu, and E. N. Wang, "Nanoengineered materials for liquid–vapour phase-change heat transfer," *Nat. Rev. Mater.*, vol. 2, no. 2, p. 16092, Feb. 2017.

[3] R. N. Wenzel, "RESISTANCE OF SOLID SURFACES TO WETTING BY WATER," *Ind. Eng. Chem.*, vol. 28, no. 8, pp. 988–994, Aug. 1936.

[4] A. B. D. Cassie and S. Baxter, "Wettability of porous surfaces," *Trans. Faraday Soc.*, vol. 40, no. 0, pp. 546–551, Jan. 1944.

[5] H. Lee, J. Shin, S. Ha, B. Choi, and J. Lee, "Frost formation on a plate with different surface hydrophilicity," *Int. J. Heat Mass Transf.*, vol. 47, no. 22, pp. 4881–4893, Oct. 2004.

[6] D. Highgate, C. Knight, and S. D. Probert, "Anomalous [`]Freezing' of water in hydrophilic polymeric structures," *Appl. Energy*, vol. 34, no. 4, pp. 243–259, 1989.

[7] A. D. Sommers, A. C. Napora, N. L. Truster, E. J. Caraballo, and C. J. L. Hermes, "A semi-empirical correlation for predicting the frost density on hydrophilic and hydrophobic substrates," *Int. J. Refrig.*, vol. 74, pp. 313–323, Feb. 2017.

[8] L. T. Li *et al.*, "Investigation of defrosting water retention on the surface of evaporator impacting the performance of air source heat pump during periodic frosting–defrosting cycles," *Appl. Energy*, vol. 135, pp. 98–107, Dec. 2014.

[9] M. A. Rahman and A. M. Jacobi, "Drainage of frost melt water from vertical brass surfaces with parallel microgrooves," *Int. J. Heat Mass Transf.*, vol. 55, no. 5, pp. 1596–1605, Feb. 2012.

[10] K. Kim and K.-S. Lee, "Frosting and defrosting characteristics of a fin according to surface contact angle," *Int. J. Heat Mass Transf.*, vol. 54, no. 13, pp. 2758–2764, Jun. 2011.

[11] M. Ezzat and C.-J. Huang, "Zwitterionic polymer brush coatings with excellent anti-fog and anti-frost properties," *RSC Adv.*, vol. 6, no. 66, pp. 61695–61702, 2016.

[12] K. A. Wier and T. J. McCarthy, "Condensation on Ultrahydrophobic Surfaces and Its Effect on Droplet Mobility: Ultrahydrophobic Surfaces Are Not Always Water Repellant," *Langmuir*, vol. 22, no. 6, pp. 2433–2436, Mar. 2006.

[13] Y.-T. Cheng and D. E. Rodak, "Is the lotus leaf superhydrophobic?," *Appl. Phys. Lett.*, vol. 86, no. 14, p. 144101, Mar. 2005.

[14] W. G. Bae *et al.*, "One-Step Process for Superhydrophobic Metallic Surfaces by Wire Electrical Discharge Machining," *ACS Appl. Mater. Interfaces*, vol. 4, no. 7, pp. 3685–3691, Jul. 2012.

[15] S. Wang, W. Zhang, X. Yu, C. Liang, and Y. Zhang, "Sprayable superhydrophobic nano-chains coating with continuous self-jumping of dew and melting frost," *Sci. Rep.*, vol. 7, p. 40300, Jan. 2017.

[16] Y. Zhang, M. R. Klittich, M. Gao, and A. Dhinojwala, "Delaying Frost Formation by Controlling Surface Chemistry of Carbon Nanotube-Coated Steel Surfaces," *ACS Appl. Mater. Interfaces*, vol. 9, no. 7, pp. 6512–6519, Feb. 2017.

[17] S. Wang, J. Zhang, X. Yu, and Y. Zhang, "Condensed dewdrops self-ejecting on sprayable superhydrophobic CNT/SiO 2 composite coating," *RSC Adv.*, vol. 7, no. 44, pp. 27574–27577, 2017.

[18] C. Lv, X. Zhang, F. Niu, F. He, and P. Hao, "From Initial Nucleation to Cassie-Baxter State of Condensed Droplets on Nanotextured Superhydrophobic Surfaces," *Sci. Rep.*, vol. 7, p. 42752, Feb. 2017.

[19] F. Wang, C. Liang, and X. Zhang, "Research of anti-frosting technology in refrigeration and air conditioning fields: A review," *Renew. Sustain. Energy Rev.*, vol. 81, pp. 707–722, Jan. 2018.

[20] S. Zhang, J. Huang, Y. Cheng, H. Yang, Z. Chen, and Y. Lai, "Bioinspired Surfaces with Superwettability for Anti-Icing and Ice-Phobic Application: Concept, Mechanism, and Design," *Small*, vol. 13, no. 48, p. UNSP 1701867, Dec. 2017.

[21] M. J. Kreder, J. Alvarenga, P. Kim, and J. Aizenberg, "Design of anti-icing surfaces: smooth, textured or slippery?," *Nat. Rev. Mater.*, vol. 1, no. 1, p. 15003, Jan. 2016.

[22] I. McCue, E. Benn, B. Gaskey, and J. Erlebacher, "Dealloying and Dealloyed Materials," *Annu. Rev. Mater. Res.*, vol. 46, no. 1, pp. 263–286, 2016.

[23] K. Sieradzki, R. R. Corderman, K. Shukla, and R. C. Newman, "Computer simulations of corrosion: Selective dissolution of binary alloys," *Philos. Mag. A*, vol. 59, no. 4, pp. 713–746, Apr. 1989.

[24] D. M. Artymowicz, J. Erlebacher, and R. C. Newman, "Relationship between the parting limit for de-alloying and a particular geometric high-density site percolation threshold," *Philos. Mag.*, vol. 89, no. 21, pp. 1663–1693, Jul. 2009.

[25] J. Rugolo, J. Erlebacher, and K. Sieradzki, "Length scales in alloy dissolution and measurement of absolute interfacial free energy," *Nat. Mater.*, vol. 5, no. 12, pp. 946–949, Dec. 2006.

[26] L. Tang *et al.*, "Electrochemical Stability of Nanometer-Scale Pt Particles in Acidic Environments," *J. Am. Chem. Soc.*, vol. 132, no. 2, pp. 596–600, Jan. 2010.

[27] J. Snyder, I. McCue, K. Livi, and J. Erlebacher, "Structure/Processing/Properties Relationships in Nanoporous Nanoparticles As Applied to Catalysis of the Cathodic Oxygen Reduction Reaction," *J. Am. Chem. Soc.*, vol. 134, no. 20, pp. 8633–8645, May 2012.

[28] A.-A. El Mel *et al.*, "Unusual Dealloying Effect in Gold/Copper Alloy Thin Films: The Role of Defects and Column Boundaries in the Formation of Nanoporous Gold," *ACS Appl. Mater. Interfaces*, vol. 7, no. 4, pp. 2310–2321, Feb. 2015.

[29] Q. Lu *et al.*, "Highly porous non-precious bimetallic electrocatalysts for efficient hydrogen evolution," *Nat. Commun.*, vol. 6, p. 6567, Mar. 2015.

[30] Q. Chen and K. Sieradzki, "Spontaneous evolution of bicontinuous nanostructures in dealloyed Li-based systems," *Nat. Mater.*, vol. 12, no. 12, pp. 1102–1106, Dec. 2013.

[31] Z. Qi and J. Weissmüller, "Hierarchical Nested-Network Nanostructure by Dealloying," *ACS Nano*, vol. 7, no. 7, pp. 5948–5954, Jul. 2013.

[32] Z. Qi *et al.*, "Porous Gold with a Nested-Network Architecture and Ultrafine Structure," *Adv. Funct. Mater.*, vol. 25, no. 17, pp. 2530–2536, May 2015.

[33] J. Erlebacher, M. J. Aziz, A. Karma, N. Dimitrov, and K. Sieradzki, "Evolution of nanoporosity in dealloying," *Nature*, vol. 410, no. 6827, pp. 450–453, Mar. 2001.

[34] Q. Yun *et al.*, "Chemical Dealloying Derived 3D Porous Current Collector for Li Metal Anodes," *Adv. Mater.*, vol. 28, no. 32, pp. 6932–6939, Aug. 2016.

[35] K.-C. Park *et al.*, “Condensation on slippery asymmetric bumps,” *Nature*, vol. 531, no. 7592, pp. 78–82, Mar. 2016.